Document Number**:** H2020-ICT-52/RISE-6G/D5.4

Project Name:
Reconfigurable **I**ntelligent **S**ustainable **E**nvironments for **6G** Wireless Networks
(RISE-6G)

Deliverable D5.4

Estimation algorithms for RIS-based localisation, mapping and sensing (Final Specifications)

Date of delivery:	29/09/2023	Version:	1.0
Start date of Project:	01/01/2021	Duration:	36 months

Deliverable D5.4
Estimation algorithms for RIS-based localisation, mapping and sensing (Final Specifications)

Project Number:	H2020-ICT-52 / 101017011
Project Name:	**R**econfigurable **I**ntelligent **S**ustainable **E**nvironments for **6G** Wireless Networks

Document Number:	H2020-ICT-52/RISE-6G/D5.4
Document Title:	Estimation algorithms for RIS-based localisation, mapping and sensing (Final Specifications)
Editor(s):	Vincenzo Sciancalepore (NEC)
Authors:	Vincenzo Sciancalepore (NEC), Benoit Denis (CEA), Henk Wymeersch (CHA), Paolo Di Lorenzo (CNIT), Stefania Sardellitti (CNIT), Francesca Costanzo (CNIT), Moustafa Rahal (CEA), Hyowon Kim (CHA), Musa Furkan Keskin (CHA), Hui Chen (CHA), Navid Amani (CHA), Radosław Bartnik (AAU), Fabio Saggese(AAU), Petar Popovski (AAU), George Alexandropoulos (NKUA), Konstantinos Katsanos (NKUA)
Dissemination Level:	PU
Contractual Date of Delivery:	29/09/2023
Security:	Public
Status:	Final
Version:	1.0
File Name:	RISE-6G_WP5_D5.4_Final.docx

Abstract

This deliverable provides the final results on the algorithms for RIS-based localisation, mapping and sensing performed within the work package 5 "RIS for Enhanced Localisation and Sensing" of the RISE-6G project.

Keywords

Beyond-5G; 6G; RIS; Localisation; Sensing; Connectivity

Contents

List of Figures

List of Tables

List of Acronyms

5G-NR	5th Generation - New Radio
5G-PPP	5G infrastructure Public Private Partnership
AMF	Access and Mobility management Function
AoA	Angle of Arrival
AoD	Angle of Departure
AML	Approximate maximum likelihood
AMML	Approximate mismatched maximum likelihood
AU	Active User
BP	Belied Propagation
BS	Base Station
CAPEX	CAPital EXpenditure
(C)CDF	(Complementary) Cumulative Density Function
CF	Closed-Form
CPU	Central Processing Unit
CR(L)B	Cramér-Rao (Lower) Bound
CS	Cadidate Site
CSI	Channel state information
DAE	Denoising Autoencoder
DBSCAN	Density-Based Spatial Clustering of Applications with Noise
DL	Downlink
DL-DoD	Downlink Direction of Departure
DL-TDoA	Downlink Time Difference of Arrival
DoA	Direction of Arrival
DoD	Direction of Departure
DQfD	Deep Q-learning from Demonstrations
DQL	Deep Q-Learning
D-RISA	Deep RIS-Aware
DRL	Deep Reinforcement Learning
(E)KF	(Extended) Kalman Filter
EM	Electromagnetic
EMF	Electro Magnetic Field
ES	Exhaustive Search
FF	Far-field
FFT	Fast Fourier Transform
FIM	Fisher information matrix
FMCW	Frequency Modulated Continuous Wave
GDoP	Geometric Dilution of Precision
GLRT	Generalized Likelihood Ratio
GOSPA	Generalized Optimal Sub-pattern Assignment
GS	Grid Search
IFFT	Inverse Fast Fourier Transform
ITU	International Telecommunication Union
JLFD	Joint Localisation and Failure Diagnosis
JrCUP	Joint RIS Calibration and User Positioning
LB	Lower Bound
kNN	k-Nearest Neighbour
KPI	Key-Performance Indicator
LB-AoI	Localisation Boosted - Area of Influence
LE-AoI	Localisation Enabled - Area of Influence
LIS	Large Intelligent Surfaces
LMF	Location Management Function
LOF	Local-Outlier-Factor
LoS	Line-of-Sight
LTE	Long Term Evolution

MAP	Maximum A Posteriori
MC	Multicarrier
MCC	Maximum Correlation Coefficient
MD	Minimum Distance
MF	Matched Filter
MIMO	Multiple Inputs Multiple Outputs
ML(E)	Maximum Likelihood (Estimator)
MLP	Multi-Layered Perceptron
MMSE	Minimum Mean Squared Error
MP	Message Passing
MPC	Multipath Component
MCRB	Miss-specified Cramer Rao Bound
MTBF	Mean Time Between Failures
NF	Near-field
NLoS	Non-line-of-sight
NMSE	Normalized Mean Squared Error
NN	Neural Network
NVAA	Non-Value-Added Activities
OFDM	Orthogonal Frequency Division Multiplexing
OMP	Orthogonal Matching Pursuit
OPEX	OPerating EXpenditure
PDF	Probability Density Function
PEB	Position error bound
PF	Particle Filter
PMB	Poisson multi-Bernoulli
ReLU	Rectified Linear Unit
RF	Radio Frequency
RMap	Radio Mapping
R-RIS	Reflective RIS
RT-RIS	Reflective-transmission RIS
RIS	Reconfigurable Intelligent
RISC	RIS controller
RISO	RIS orchestrator
RMSE	Root Mean Square Error
RPCA	Robust Principal Component Analysis
RRIS	Reflective RIS
RSSI	Received Signal Strength Indicator
RTT	Round Trip Time
RT-ToF	Round Trip – Time of Flight
Rx	Receiver
RM	Radio Map
SAA	Small Angle Approximation
SAGE	Space-Alternating Generalized Expectation-maximization
SCA	Successive Convex Approximation
SDR	Software Defined Radio
SISO	Single Input Single Output
SLAM	Simultaneous Localisation and Mapping
SNCF	Société Nationale des Chemins de Fer français
SP	Scattering Point
SNR	Signal-to-noise ratio
TDoA	Time Difference of Arrival
ToA	Time of Arrival
TP	Test Points
TRIS	Transmit-RIS
Tx	Transmitter
UAV	Unmanned Aerial Vehicle

UE	User Equipment
UTDoA	Uplink Time Difference of Arrival
UL	Uplink
UL-DoA	Uplink Direction of Arrival
UL-TDoA	Uplink Time Difference of Arrival
VA	Virtual Anchor
VEB	Velocity Error Bound
WB	Wideband
WFL	Wireless Fingerprinting Localisation
(W)LS	(Weighted) Least Squares

1 Introduction

The RISE-6G project is one of the 5G infrastructure Public Private Partnership (5G-PPP) projects under the European Commission's Horizon 2020 framework. The focus of the project is to design, prototype, and trial radical technological advances based on reconfigurable intelligent surfaces (RISs) to forge a new generation of dynamically programmable wireless propagation environments. RISs will both enable and boost connectivity, localisation, and sensing performance, as well as adapt to dynamic requirements on electromagnetic field emissions, energy efficiency, and secrecy.

Within RISE-6G, work package 5 (WP5) considers exploiting RIS for improved localisation, sensing and mapping performances. The aim of WP5 is two-fold: (i) to develop localisation-oriented network architecture for RIS deployment and profile control to optimise the aforementioned features' key performance indicators (KPIs); (ii) to develop and evaluate detection and estimation algorithms that enable RIS-based localisation and sensing, for localising connected wireless devices, building dynamic environments and radio maps, as well as passively sensing physical features.

1.1 Deliverable objectives

This document provides the final results related to Task 5.2 from WP5 and contains a summary of relevant contributions developed within that work package.

After providing control and architectural building blocks in D5.3 [RISED53] as result of the T5.1, hereafter we provide the following research items to enable RIS-empowered networks where boosted cm-level environmental awareness is provided even in highly obstructed conditions. In particular, this deliverable complementarily builds on top of Deliverable D5.2 [RISED52], which already accounted for former and/or initial contributions. Such contributions are hereafter recalled for the sake of completeness but not necessarily detailed herein, while focusing mostly on new material and results.

Estimation of location-dependent multipath parameters: This item involves the development of suitable algorithms for estimating multipath characteristics that vary with location. Such characteristics encompass parameters like multipath delays, power levels, departure and arrival angles, and Doppler shifts. The approach includes methods that are designed to work with partial or imperfect prior Channel State Information (CSI) for both the end-to-end and side RIS channels, both in the initial setup phase and during steady-state tracking. Furthermore, advanced beam-training strategies are explored, particularly those leveraging prior mobile location information. This research item is addressed by set of contributions A, as listed in Section 3.2.

Estimation of active UEs and passive objects: This item focuses on identifying and locating active Users Equipment (UEs) and passive objects in a RIS-empowered communication environment (Smart Radio Environment). One set of methods leverages the location-dependent channel parameters and radio metrics obtained through the techniques mentioned earlier. Another set aims to directly perform positioning without intermediate channel estimation steps by analysing the received signals. This comprehensive approach allows for a versatile and efficient localisation process. All proposals are listed as set of contributions B, as listed in Section 3.3.

RIS-enabled SLAM: In this item, the objective is to develop algorithms with low computational complexity that can simultaneously solve two fundamental challenges: simultaneous Localization and Mapping (SLAM) and opportunistic (and integrated) sensing. This is accomplished by relying on RIS-enabled communication links connecting the Base Station (BS) and UEs. These solutions are designed to deliver high nominal accuracy even in the presence of generalized Non Line of Sight (NLoS) conditions, while also mitigating multipath interference introduced by RISs. List of such contributions is marked as set of contributions C in Section 3.4.

Spectrum sensing, Radio Frequency (RF) mapping and fingerprinting localisation: This item involves conducting wireless activity sensing with extremely high resolution, down to the

centimetre-level. Additionally, it enables a technique known as wireless fingerprinting localisation (WFL) that utilises existing network infrastructure like WiFi or cellular networks for localisation, offering an effective and practical means of achieving high-precision localisation without the need for extensive additional hardware deployment. This approach has the potential to significantly enhance location-based services and applications. Such contributions are listed as set of contributions D in Section 3.5.

Algorithms and techniques here presented serve as an input to WP7, where a subset of methods will be implemented and used in proof-of-concept validations relying on real hardware as further detailed in Section 4.

1.2 Deliverable structure

The deliverable is structured as follows.

Section 2 provides the foundations of localisation and sensing techniques against conventional approaches where RISs are not in place. Section 3 focuses on the proposed algorithms to estimate localisation and sensing features. In particular, four different sets of contributions are provided: *i*) contributions on multi-mode parameter estimation, *ii*) algorithms on UE location estimation, *iii*) passive object detection techniques and *iv*) overview of spectrum sensing, RF mapping and fingerprinting empowered by AI. Section 4 sheds the light on the interaction with in-lab and on-field demonstrations expected to be detailed and published within the Deliverable 7.3 (WP7). Lastly, Section 5 draws concluding remarks of the document.

2 Localisation and Sensing

The purpose of this section is to provide an overview of the principles of radio localisation and sensing methods by shedding the light on the ad-hoc use of reconfigurable intelligent surfaces (RISs) as a mean to provide opportunistic boosted cm-level environmental awareness, including joint mobile position, mapping and sensing functionalities.

Architectural details and corresponding control mechanisms are more deeply discussed in deliverable D5.1 [RISED51] and D5.3 [RISED53].

2.1 Foundations of localisation

In the context of radio systems, localisation (synonym: positioning) is the process of determining the 2D or 3D location of a connected device (UE), based on uplink (UL) or downlink (DL) measurements with respect to several BSs [PRL+18]. The measurements are performed based on the reception of dedicated pilot signals and can be of the forms described in Table 2-1. Observe that a combination of angle and delay measurements can be used for UE localisation and that different measurement combinations put different requirements on both the number of BSs as well as on their mutual synchronization [KDA+22]. For this latter reason, pure Time-of-Arrival (ToA) measurements with a UE synchronized to a BS is impractical in real scenarios, since even small synchronization errors lead to large localisation errors (e.g., 10 ns clock error corresponds to 3 meters error). Examples of two different measurement settings for localisation are shown in Figure 2-1.

Table 2-1 Localisation measurements and requirements for 3D positioning.

Measurement	UL or DL	Number of BSs needed	Comment
Time-of-arrival (ToA) of the first path	Either	3	BSs should be synchronized with the UE
Time-difference-of-arrival (TDoA), derived from several ToA measurements	Either	4	BSs should be mutually synchronized
Round-trip-time (RTT), derived from several ToA measurements	Both	3	No synchronization needed
Angle-of-arrival (AoA)	UL	2	Requires planar arrays at each BS
Angle-of-departure (AoD)	DL	2	Requires planar arrays at each BS
TDoA+UL-AoA	UL	2	BSs should be mutually synchronized
RTT+ UL-AoA	Both	1	No synchronization needed
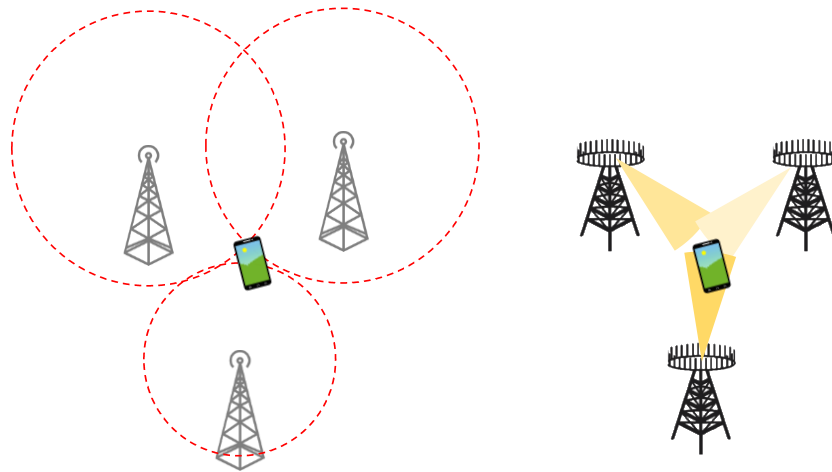
Figure 2-1. Example of RTT-based localisation (left), constraining the UE on the intersection of circles (2D) or spheres (3D). On the right, an example of localisation based on DL-AoD measurements, constraining the user within a sector of each BS.

The pilots used for localisation are tailored in time, frequency, and space. In time-frequency, so-called comb signals are used, which occupy the entire signal bandwidth while allowing orthogonality across BSs [3GPP10]. In space, the time-frequency signals are repeated for different directional beams at the BS, while providing angle measurements (AoA in UL or AoD in DL). The quality of the ToA and AoA/AoD measurements depends on several factors [WLW+18]:

- **Bandwidth:** the amount of available bandwidth is directly related to delay resolution and thus to multipath suppression (in particular, two paths can be resolved if their delay difference is at least 1 over the bandwidth). If strong signal paths are present, say, 10 meters after the direct path, then a bandwidth of around 30 MHz is needed to resolve this secondary path. For that reason, a large bandwidth is important for accurate localisation in cluttered environments.

- **Transmission power:** the accuracy of delay and angle measurements depends on the received signal-to-noise ratio (SNR), which is itself proportional to the transmission power. Hence, higher transmit powers lead to more accurate localisation, provided multipath can be resolved. Since localisation depends on pilot signals, an increase in SNR can also be achieved through longer transmission times.

- **Number of antennas:** similar to bandwidth being related to delay resolution, so is the number of antennas proportional to angle resolution (the relation for a linear array is that two paths with angle difference (in radians) beyond 2/(number of antennas) can be resolved). Hence, a larger array of half-wavelength spaced elements leads to improved angular resolution, which can be traded off against delay resolution.

- **Signal processing and hardware limitation:** depending on the computational capacity and knowledge regarding the utilised beams, the delay and angle estimation performance can be improved. Moreover, hardware and calibration errors (e.g., synchronisation errors) significantly affect localisation performance, leading possibly to a significant gap between theory and practice.

2.2   Foundations of sensing

In contrast to localisation, 3GPP has until now not offered any support for radar-like sensing. Such sensing is conventionally broken down as [WSD+21]:

- **Monostatic sensing:** a transmitter (Tx) and a receiver (Rx) are co-located and share a common clock. The Tx emits a waveform, known to the Rx. The Rx processes the backscattered waveform to detect the presence of targets (static or dynamic object), as well as their distance, bearing, and velocity. Such type of radar sensing is commonly

employed in automotive radar, and requires dedicated waveforms, shaped in time and frequency (e.g., frequency modulated continuous wave (FMCW) [LLH+16] [SFS+18]) with orthogonality across transmit antennas, to provide a large virtual aperture. FMCW-type waveforms have a constant envelope, making them hardware-friendly. In the context of communication systems, standard data-bearing signals can be used (e.g., orthogonal frequency division multiplexing (OFDM)) [CKA+20]. Monostatic sensing requires a full-duplex receiver.

- **Bistatic sensing:** in this mode, Tx and Rx are not co-located and do not share a common clock. Pilot signals are emitted by the Tx and the backscattered signal is processed by the Rx. The lack of synchronization requires a clock reference, which can be offered by the direct path between Tx and Rx.

- **Multistatic sensing:** this is a generalization of bistatic sensing with several Rx. The information for the different Rxs must be fused to provide an overall picture of the detected objects. The larger number of Rxs allows for higher resolution, due to the increased aperture, provided the Rxs are synchronized.

The discussion related to delay and angle resolution, as well as signal processing and hardware limitations from Section 2.1 is still relevant. In terms of power, it is important to note that sensing is subject to more severe path loss than localisation, as the signal scatters from objects before reaching the Rx.

2.3 RIS in localisation and sensing

RISs have potential to improve localisation and sensing performance, when added to conventional deployments [WHD+20]. This is referred to as 'boosting'. In addition, RIS also have the potential to provide location estimates to UEs when conventional deployments fail. This is referred to as 'enabling'.
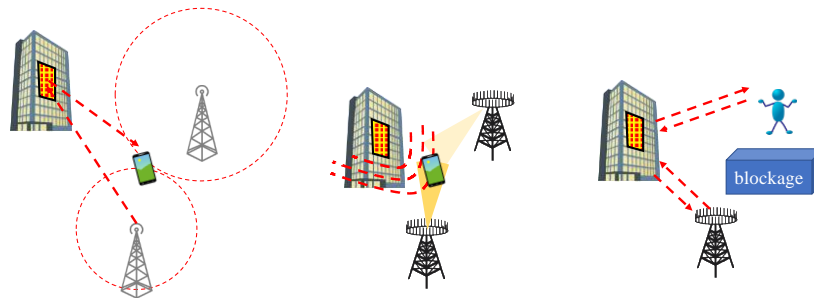
Figure 2-2. Examples of use of RIS in localisation: a new signal path via a RIS and a new reference by the RIS (left); large RIS provides wavefront curvature for localisation measurements (middle); a RIS provides a signal path to avoid signal blockage in monostatic sensing.

In wireless systems, RISs can boost or enable user localisation by providing the following features (see Figure 2-2):

1. **New signal path**: The reflected signal from the RIS provides the Rx with an additional signal path whose parameters can be estimated and used for localisation. Compared to other multipath generated by the scatterers, the path from the RIS is stronger due to the multitude of RIS elements and beamforming gain.

2. **New location references**: RISs, when used as a part of wireless infrastructure, have a fixed location and orientation. Therefore, they provide a location reference that can be used to estimate the unknown location of the user. This separates RISs from scatterers in the environment as the location of the scatterers are often unknown.

3. **Near-field (NF) measurements:** Since the dimensions of RISs are much larger than the conventional planar arrays used in Multiple Inputs Multiple Outputs (MIMO) systems, and they can be installed close to the user site, it is probable that the user falls within

the near-field of the RIS [DNA+21]. In the near-field, one can also use the phase of the received signal to directly estimate the location of the user.

In Table 2-2, we present some of the scenarios where the user localisation in 3D is possible for wireless systems equipped with RISs. Here we only consider single-antenna BSs.

Table 2-2 RIS Localisation measurements and requirements for 3D positioning.

Measurement	UL or DL	# BSs	#RISs	Comment
ToA + AoD	Both	0	1	No synchronisation needed (only a coarse synchronisation between transmitted pilots and RIS configurations).
TDoA + AoD	Either	1	1	No synchronisation needed
AoD	Either	1	2	No synchronisation needed

3 Estimation algorithms proposals

3.1 Motivations and challenges

As defined and detailed in [RISED52], localisation is carried out through a meticulous two-step procedure. The initial step encompasses a channel parameter estimation routine, which serves the dual purpose of discerning the quantity of discernible signal paths and extracting critical information such as Time of Arrival (ToA), Angle of Arrival (AoA), and Angle of Departure (AoD) for each of these paths. In the subsequent phase, the Line of Sight (LoS) path is identified and selected for localisation purposes. This selection is typically based on criteria like the shortest signal delay or the highest channel gain. In contrast, the remaining signal paths are either excluded from further consideration or utilized to augment the localisation process by contributing to the mapping of the target's position.

There is a large body of literature on such parametric channel estimation, including ESPRIT [RHD14], generalized approximate message passing [BSY19], orthogonal matching pursuit [SGD+17] and RIMAX/SAGE [TLR04]. Note that channel parameter estimation is distinct from (unstructured) channel estimation [BG06], which aim to determine the complete channel matrix or vector, based on pilot transmissions. This unstructured channel estimate is usually an input for parametric channel estimation. Unstructured channel estimation is used in the context of localisation for fingerprinting. Therefore, the estimated path parameters should be accompanied with associated uncertainties, prior to performing localisation.

Hereafter, we list the set of contributions highlighting (in *italic* font in Table 3-1, Table 3-2, Table 3-3 and Table 3-4) only the changes with the respect to the previously introduced contributions, as per D5.2 [RISED52]. These contributions are collected in the following sets:

- *Set A*: 9 contributions related to channel parameter estimation (Section 3.2).

- *Set B*: 9 contributions related to active UE location estimation (Section 3.3).

- *Set C*: 5 contributions related to SLAM and passive object detection (Section 3.4).

- *Set D*: 4 contributions related to spectrum sensing, RF mapping and fingerprinting (Section 3.5).

3.2 Set of contributions #A

Table 3-1 An overview of parameter estimation contributions

Architecture	Cont. #A-1: Far-field ToA and AoD estimation of a signal reflected by a RIS	Cont. #A-2: Far-field ToA and AoD estimation in full-duplex of a signal reflected by a RIS	Cont. #A-3: Near-field ToA and AoD estimation of a signal reflected by a RIS	Cont. #A-4: AoA estimation at a sensing RIS	*Cont. #A-5: RIS-enabled veolcity estimation in near-field*
Nr BS	1	0	1	0	1
Nr RIS	Multiple	1	1	1	1
Nr UEs	Multiple	1	1	1	1
UE Mobility	Stationary	Stationary	Stationary	Stationary	Mobile
RIS Type	Reflective	Reflective	Reflective	Sensing	Reflective
Setup					
Uplink/Downlink	Downlink	Uplink	Downlink	Uplink	Downlink
Indoor/outdoor/UAV	Outdoor	Outdoor	Indoor and outdoor	Indoor and outdoor	Indoor/outdoor
Frequency Band	30 GHz	28 GHz	28 GHz	30 GHz	28 GHz or sub-6 GHz
Narrowband/wideband	Wideband	Wideband	Narrowband	Narrowband	Narrowband
Near field/far field	Far field	Far field	Near field	both	Near field

	LoS (Tx-Rx) and NLoS (Tx-RIS-Rx)	LoS (UE-RIS-UE)	NLoS	RIS-UE	NLoS
LoS/NLoS (BS-RIS-UE)					
Imperfections or other hardware considerations	-	-	Phase-dependent RIS amplitude variations	-	Single antenna BS and UE
Measurement type	ToA and AoD	ToA and AoD	ToA and AoD	AoA	ToA, AoD, channel gain (intermediary/approximate)
RIS configuration strategy	Random profile	Directional profile	Random profile	DFT or Random	Random, directional and extended to optimal
Who collects measurements	Rx	UE	UE	RIS	BS
Synchronisation	Unsynchronized	-	No	No	Unsynchronized

Architecture	*Cont. #A-6: Channel parameter estimation for joint RIS calibration and user positioning (channel estimation in Cont. #B-9*	*Cont. #A-7: Channel parameter estimation for Multi-RIS-Enabled 3D Sidelink Positioning (channel estimation in Cont. #B-10)*	*Cont. #A-8: 3D Localisation with distributed passive RISs and blocked BS access*	*Cont. #A-9: Localisation via a single partially connected receiving RIS*
Nr BS	1	0	1	0
Nr RIS	1	Multiple	Multiple	1
Nr UEs	1	Multiple	1	1
UE Mobility	Stationary	Stationary	Stationary	Stationary
RIS Type	Active	Reflective	Reflective	Receiving
Setup				
Uplink/Downlink	UL	DL	UL	UL
Indoor/outdoor/UAV	Outdoor/UAV	Outdoor	Outdoor	Indoor/Outdoor
Frequency Band	28 GHz	28/60 GHz	28 GHz	28 GHz
Narrowband/wideband	WB	WB	Narrowband	Narrowband
Near field/far field	FF	FF	Far field	Far field
LoS/NLoS (BS-RIS-UE)	LoS and NLoS	LoS RIS-UE and LoS UE-UE	NLoS	LoS
Imperfections or other hardware considerations	-	-	-	-
Measurement type	ToA, AoA, Spatial frequency	AoD, AoA, spatial frequency	AoA	AoA
RIS configuration strategy	Random	Random, directional, and derivative codebook	Random	Random, Directional
Who collects measurements	BS	UE	BS	RIS
Synchronisation	Unsynchronized	Unsynchronized	Unsynchronised	Unsynchronised

#A-1: Far-field ToA and AoD estimation of a signal reflected by a RIS

Please refer to D5.2 [RISED52] for an extended description of this contribution.

#A-2: Far-field ToA and AoD estimation in full-duplex of a signal reflected by a RIS

Please refer to D5.2 [RISED52] for an extended description of this contribution.

#A-3: Near-field ToA and AoD estimation of a signal reflected by a RIS

Please refer to D5.2 [RISED52] for an extended description of this contribution.

#A-4: AoA estimation at a sensing RIS

Please refer to D5.2 [RISED52] for an extended description of this contribution.

#A-5: RIS-enabled velocity estimation in near-field

Motivation and context

A few contributions from the recent literature have addressed the impact of mobility on RIS-aided UE state estimation. For instance, in [KKS+22] the authors performed snapshot position estimation of a mobile UE under spatial-wideband effects. In [CJY+22], the utilisation of Doppler information was introduced to enable a mobile UE localisation. Then shifting away from snapshot estimation, in [GGD+21], a UE transmitting a narrowband signal is tracked through filtering (i.e., including 3D velocity as estimated variable, besides 3D position), while exploiting phase and amplitude observations accounting for the curvature-of-arrival of the impinging wavefront at a RIS in receiving mode in the Fresnel region (w.r.t. the UE). Moreover, in [AS22] the authors present an extended Kalman filter positioning and tracking algorithm to localise users with the aid of RIS while [PGA+23] develops a joint RISs reflection coefficients and BS precoder optimization problem in a single-mobile UE multi-RIS MIMO scenario in the NF domain and estimates the UE's trajectory. And finally, in [XYS22], velocity is estimated in FF LoS conditions via a reflective RIS, while relying on both direct and RIS-reflected paths.

In contrast with the previous contributions, one aim here is simply to exploit the small-scale Doppler effects induced by UE mobility (i.e., over the short time duration of a sequence of DL pilot signals) at the different elements of a large reflective RIS to enable "snapshot" velocity estimation, given a known prior UE location and a coarse initial guess. Regarding this estimation problem, the theoretical velocity error bound (VEB) was initially derived in [RISED52] for benchmark purposes.
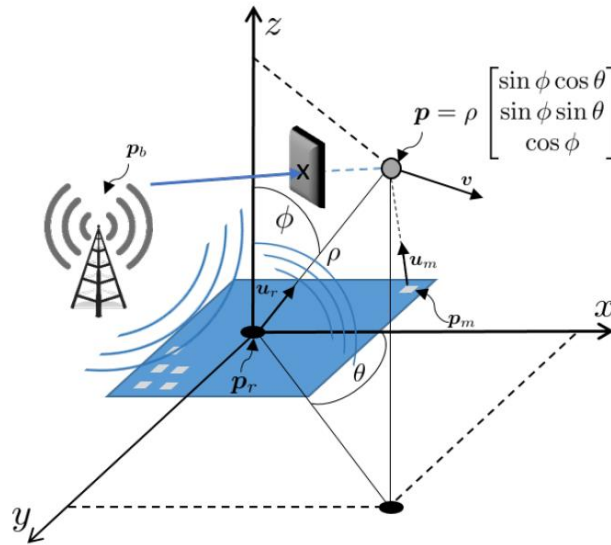
Figure 3-1. Considered scenario and problem geometry for RIS-aided position-based user velocity estimation over DL pilots transmission in NF NLoS conditions.

Methodology

To handle the previous RIS-aided position-based velocity estimation problem, a dedicated iterative refinement routine has been proposed, as follows (please refer to Figure 3-1).

- Applying linearisation and small angle approximations, this procedure first relies on an expression approximating the response of the reflective RIS under UE mobility in NF, as a function of a residual velocity term that accounts for the latest velocity estimation error (typically, from a previous estimation step).

- Then, this approximated RIS response is plugged into a simplified formulation of the likelihood maximization problem, which is further solved with respect to both the velocity residual and channel gain of the reflected path, by alternating updates over the two optimization variables thanks to two simple closed-form solutions.

Results and discussion

The performance of the proposed position-based velocity estimation approach was evaluated through Monte-Carlo simulations and compared with the corresponding theoretical VEB from [RISED52], while illustrating the impact of key parameters such as the RIS-UE distance in light of geometric NF conditions, or the actual velocity module.

Results in Figure 3-2 show that the algorithm of estimating the UE's 3D velocity knowing the position attains the theoretical bounds at close and far distances. We also applied a global refinement routine as a precaution to further enhance the estimation in case the algorithm fails. As expected, it is hence noticed that both the VEB and estimation performance degrade with larger RIS-UE distances.
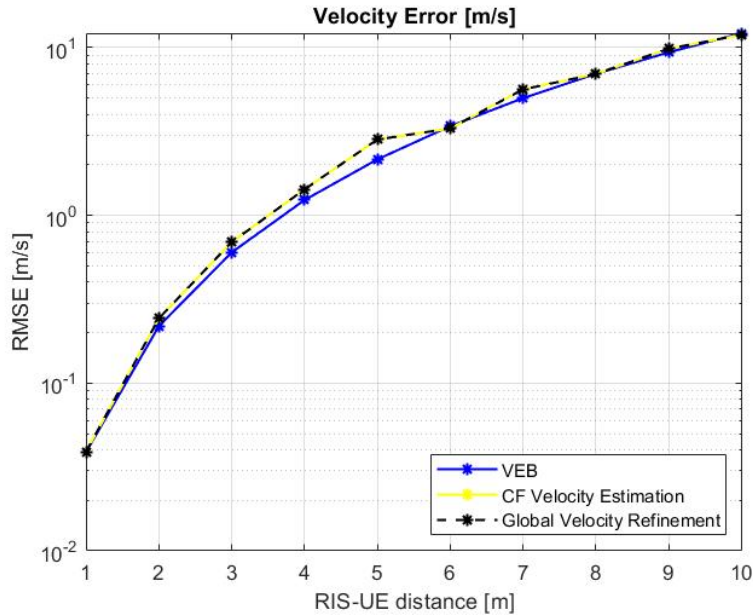
Figure 3-**2**. **Root Mean Square Error (RMSE) of velocity estimation for a known UE position and v = 1 m/s, along with the corresponding VEB, versus RIS-UE distance.**

Perspective and relation to other WP5 contributions

The RIS-aided position-based velocity estimation approach described above can be extended/generalized into a joint velocity-position snapshot estimation scheme with no prior information (i.e., performing blind 6D state estimation), while still benefiting from the same small-scale Doppler effects induced with respect to the RIS elements in NF (See contribution #B-6 below).

#A-6: Channel parameter estimation for joint RIS calibration and user positioning

Motivation and context

Recent studies have shown the potential of RIS-assisted localisation systems in various scenarios, e.g., localisation under user mobility [KKS+22], joint localisation and synchronization [FKS+22], simultaneous indoor and outdoor localisation [HFA22], received-signal-strength based localisation [ZZD+21], and so on. Although promising results on RIS-assisted localisation are shown in the literature, most of the existing research works regard RIS as an anchor with known position and orientation, which is not realistic in some application scenarios such as fixed RISs with calibration error and mobile RISs. As a matter of fact, calibration errors in the RIS placement and geometric layout are unavoidable in practice, making RIS calibration a necessity for performing a high-precision localisation. In this work, we consider a far-field joint RIS calibration and user positioning (JrCUP) scenario under an uplink SIMO system, as shown in Figure 3-3. More specifically, a UE is sending positioning pilot signals to a BS through the LoS path and RIS path, and we want to estimate the 3D position and 1D orientation of a RIS ($\mathbf{p}_R$, o_3), 3D position of the UE ($\mathbf{p}_U$), and the clock offset between the UE and the BS (Δ).
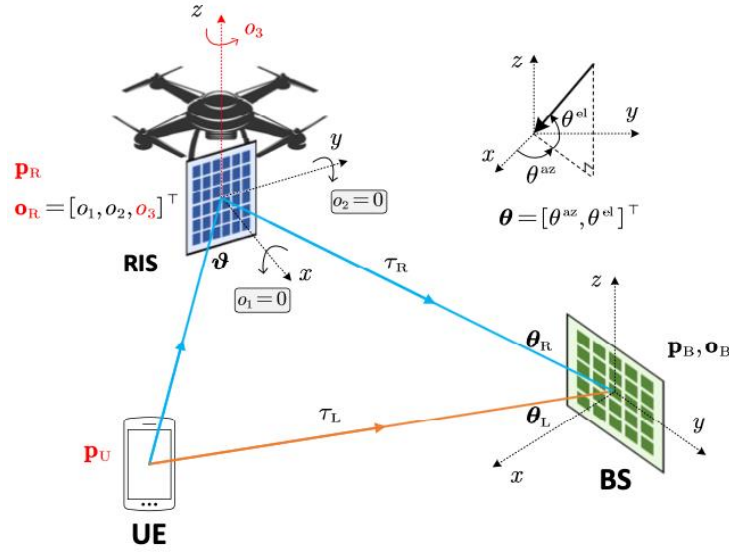
Figure 3-3. Illustration of an uplink SIMO JrCUP scenario, where the states of the UE and RIS are unknown. The RIS is deployed on a drone with gravity sensors, where the RIS is always perpendicular to the ground; hence, only one orientation angle needs to be estimated.

Methodology

To obtain these state parameters, channel parameter estimation is performed using tensor ESPRIT to extract the delay and AoA of the UE-BS channel (τ_{L}, $\boldsymbol{\theta}_{\mathrm{L}}$), delay and AoA of the UE-RIS-BS channel (τ_{R}, $\boldsymbol{\theta}_{\mathrm{R}}$), as well as two spatial frequency parameters ($\boldsymbol{\vartheta} = [\vartheta_2, \vartheta_3]$) consisting of the AoA (ϕ_A^{az}, ϕ_A^{el}) and AoD (ϕ_D^{az}, ϕ_D^{el}) information at the RIS ($\vartheta_2 = \sin(\phi_A^{az})\cos(\phi_A^{el}) + \sin(\phi_A^{az})\cos(\phi_A^{el})$, $\vartheta_3 = \sin(\phi_A^{el}) + \cos(\phi_D^{el})$).

For delay estimation, element-space tensor ESPRIT is adopted [HRD08]. Considering the hybrid structure of BS (i.e., the number of radio frequency chains is less than the number of antennas) and the passive property of the RIS (i.e., operating like an analog array), beamspace tensor ESPRIT is adopted [WSY20]. More details can be found in [ZCB+23], resulting in coarse channel parameters. After that, channel parameters are refined via least squares (LS).

Results and discussion

Figure 3-4 shows the evaluation of the RMSEs of $\boldsymbol{\theta}_{\mathrm{L}}$, $\boldsymbol{\theta}_{\mathrm{R}}$, τ_{L}, τ_{R}, and $\boldsymbol{\vartheta}$ versus the received SNR for the tensor-ESPRIT coarse estimation and LS-based refinement. The LS refinement is solved using the trust-region method and the number of iterations is set as T = 40. It is observed that the RMSEs of coarse estimation possess large gaps to the CRLBs while the proposed refinement significantly reduces the distance to the CRLBs when the received SNR is 10dB or higher. Nevertheless, there are still non-negligible gaps between the results of LS refinement (especially for $\boldsymbol{\theta}_{\mathrm{L}}$, $\boldsymbol{\theta}_{\mathrm{R}}$, and τ_{L}) and the theoretical bounds, which result from the mismatch between the used LS criterion and the actual statistics of the noise.
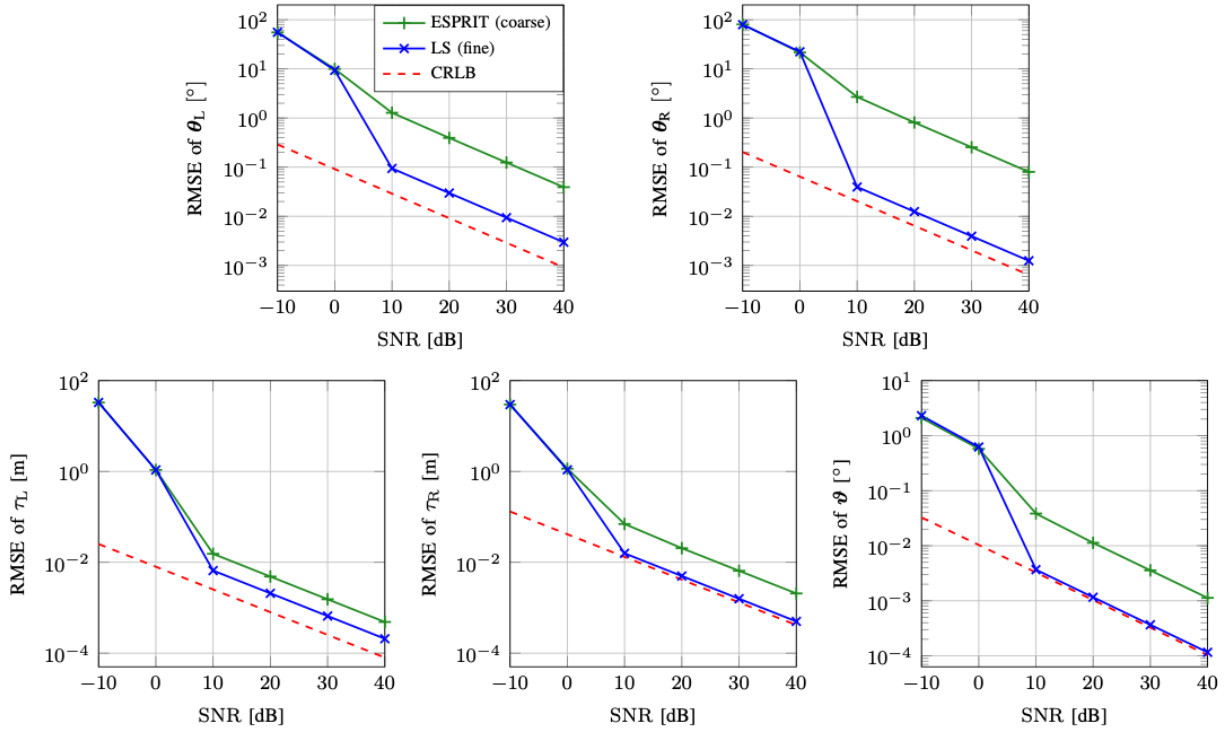
Figure 3-4. The evaluation of RMSE of channel parameters versus received SNR for the tensor-ESPRIT coarse estimation and LS-based refinement.

Perspective and relation to other WP5 contributions

In most of the localisation and sensing scenarios, RISs are treated as an anchor with known position and orientation. However, the calibration phase is usually neglected. The scenario and method proposed in this work provides a practical RIS calibration solution, benefiting other RIS-aided localisation and sensing works. The channel estimation algorithm using tensor ESPRIT can also be implemented in other RIS-involved scenarios.

#A-7: Channel parameter estimation for multi-RIS-enabled 3D sidelink positioning

Motivation and context

Positioning is expected to support communication and location-based services in the fifth/sixth generation (5G/6G) networks. With the advent of reflective RISs, radio propagation channels can be controlled, making high-accuracy positioning and extended service coverage possible. However, the passive nature of the RIS requires a signal source such as a BS, which limits the positioning service in extreme situations, such as tunnels, dense urban areas, or complicated indoor scenarios where 5G/6G BSs are not accessible. In this work, we show that with the assistance of (at least) two RISs and sidelink communication between two UEs, the absolute positions of these UEs can be estimated in the absence of BSs. In the channel estimation step, we adopt orthogonal RIS profiles to extract the spatial frequencies of the RIS channel (e.g., $\xi_\ell = \sin(\phi_{A,\ell})\cos(\theta_{A,\ell}) + \sin(\phi_{D,\ell})\cos(\theta_{D,\ell})$, $\zeta_\ell = \sin(\theta_{A,\ell})\cos(\theta_{D,\ell})$), and delays of the LOS channel (τ_0) and RIS channel (e.g., τ_ℓ for the ℓth).

Methodology

We assume the RIS profiles (or codebooks) are always known at the UE side via RIS-aided positioning protocols. To assist channel parameter estimation, we adopt time-orthogonal RIS

profiles to differentiate independent RIS paths from the others [KKS+22]. After coherent combining across different subcarriers, 1D Fast Fourier Transform (FFT) can be adopted to extract the delay information of each separated path. Then a 2D search (e.g., 2D FFT) can be performed based on the estimated delay to extract the spatial frequency of each RIS path. Unlike the channel parameter estimation using ESPRIT where the rotation invariant property needs to be satisfied, time-orthogonal RIS profiles provides flexibilities in designing RIS profiles.
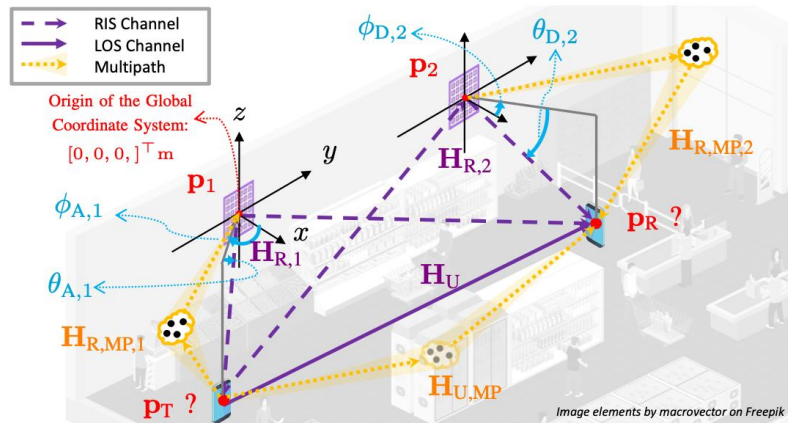
Figure 3-5. Illustration of multi-RIS-enabled 3D sidelink positioning. With the help of multiple (at least two) RIS anchors, the positions of both UEs (with respect to the global coordinate system) and the clock offset between them can be estimated through a one-way sidelink communication.

Results and discussion

We evaluate the performance of the channel estimator with a single scattering point (SP) located at $[0, 2, 3]^T$m (providing M = 3 MPCs with radar cross section coefficient of $c_{\mathrm{RCS}} = 0.5m^2$. The result of channel parameter estimation is shown in Figure 3-6. It can be seen that the coarse estimations saturate to a certain level with the increased transmit power. However, when refinement processes are applied, the Cramer Rao Lower Bounds (CRLBs) of channel parameters can be attained when the transmit power is higher than 16 dBm. Note that when transmit power is low, coarse position results may perform better due to the constrained searching area, while the refinement process does not have such constraints (usually treated as no-information regions).
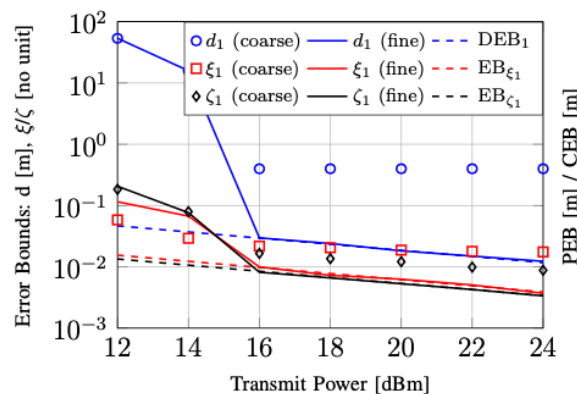
Figure 3-6. RMSE of the channel parameter estimation results vs. derived CRBs.

Perspective and relation to other WP5 contributions

The FFT-based channel estimation method provides a low-complexity estimation solution. However, to maintain the orthogonality for multiple RISs, coordination overhead should be considered, especially in the mobile scenario where coherence time is shorter.

#A-8: 3D localisation with distributed passive RISs and blocked BS access

Motivation and context

3D localisation is impossible to be achieved by only a single RIS in a considered system, based on angular parameters' measurements, such as AoAs and/or AoDs. Although promising multi-RIS-assisted 3D localisation methods are proposed in the literature [AVW22], the necessary backhaul links to connect all RISs to a fusion centre, lead to increased orchestration complexity and deployment cost. Differently from such approaches, to guarantee high accuracy 3D user localisation with a single multi-antenna BS, in this contribution, detailed in [HFW+23], it is proposed to design a two-stage method leveraging the multi-reflection wireless environment. In particular, in the first stage, an off-grid compressive sensing approach is deployed, to achieve the AoAs estimation associated with each RIS, followed by the second stage which is based on a maximum likelihood location estimation initialized with a least-squares line intersection technique. During both stages, none of the RISs possesses any radio-frequency chain nor baseband processing capability, leading to almost zero power consumption.

Methodology

The proposed system consists of one multi-antenna BS, multiple RISs and a single-antenna UE. At a considered timeslot t, the UE transmits the sounding reference signal s, with constant transmit power, which reaches the BS via reflections from all RISs, since the direct link (between the BS and UE) is assumed to be blocked. Assuming that the BS knows a priori the positions of all RISs, the signal received at the BS from the m-th RIS can be separated by applying a zero-forcing (ZF) filtering technique. This process leads to a sparsity-one signal recovery problem, which can be in turn solved by formulating an atomic norm minimisation problem. Then, this process is followed by the least-squares principle for mapping the AoA estimates to the 3D position of the UE.

Results and discussion

To evaluate the performance of the proposed 3D localisation scheme, we study the effect of the training overhead, as well as the impact of the numbers of BS antennas and RISs. In Figure 3-7, it can be observed that, as the transmit power of the UE increases, the positioning accuracy improves in terms of the RMSE, approaching the theoretical derived CRLB. It is also evident that increasing the training overhead from $T = 32$ to 40, slightly enhances the achievable performance. Compared to [AVW22], an additional signal propagation hop is encountered. As a result, more transmit power is required to achieve similar performance. On the other hand, by reducing the BS-RIS distance, we can minimise the performance gap between the two systems, without the need of backhaul links and a fusion centre.

In Figure 3-8, it is shown that the number of BS antennas (N) has a significant impact on the design of ZF combining matrix, which in turn affects the proposed localisation performance. As illustrated, increasing N improves both metrics and speeds up their performance convergence. From the CRLB perspective, it is obvious that a gain can be seen by this RIS addition in the setup. However, from the algorithmic point of view, a performance gain is achieved only with a large-sized BS, (e.g., for $N = 100$), due to the increased spatial filtering capability at reception.
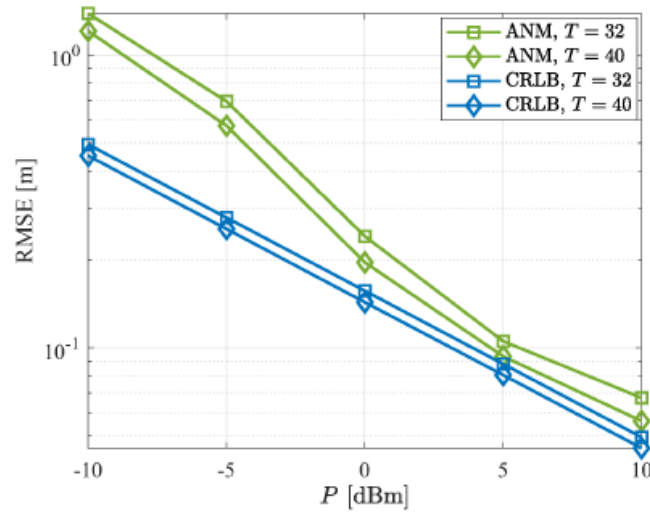
Figure 3-7. The effect of training overhead of T on the performance of the proposed 3D localisation system.
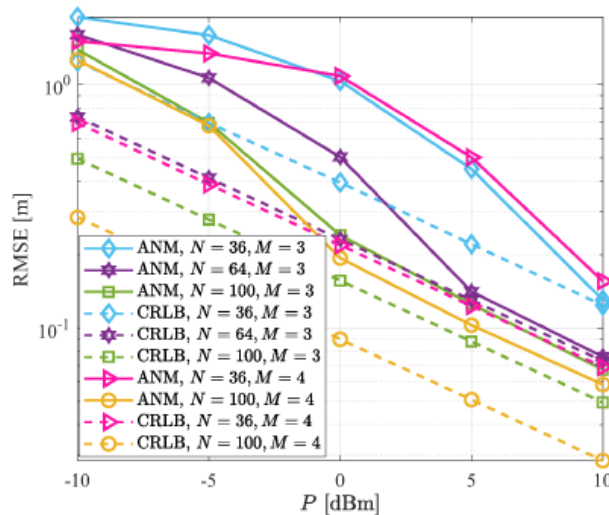
Figure 3-8. The effect of the number of BS antennas and that of RISs on the performance of the proposed 3D localisation system.

Perspective and relation to other WP5 contributions

This contribution is designed to combat the BS-UE blockage problem, which is a prominent deployment scenario for RISs. The algorithmic treatment, involving compressed sensing tools and least-squares techniques, is similar to other algorithmic approaches presented in this WP, although it is altered to fit the multi-RIS setting. Its control and signalling aspects have been discussed under contribution #C7 of D5.3 [RISED53].

#A-9: Localisation via a single partially connected receiving RIS

Motivation and context

According to the literature, it has been shown that a single mmWave BS operating over a very large bandwidth and equipped with a large number of antennas, can also achieve positioning with high accuracy. Such a BS should rely on both temporal and angular channel parameters to achieve the desired goal, at the cost of utilizing large-sized antenna arrays, as well as large

communications signal bandwidths. In [AVW22], it has been shown that multiple spatially distributed RISs are capable to collect measurements that can be helpful to perform highly accurate 3D localisation, although at a large deployment cost and implementation complexity. In this contribution, capitalizing on the localisation framework of [AVW22], a partially-connected receiving RIS (R-RIS) hardware architecture is proposed comprising a few co-located single-RX-RF RIS subarrays, targeting at 3D localisation in a computationally autonomous manner, that is, without the intervention of any BS or access point (AP).

Methodology

We consider that the R-RIS consists of single-RX-RF UPAs of meta-atoms placed parallel to the yz plane. In addition, the outputs of the reception RF chains of all subarrays feed a baseband AoA estimation and localisation module, which is based on the extraction of the impinging signal's angular parameters with respect to each subarray. Capitalizing on theoretical analyses related to the CRLB on the channel parameters estimation, the effect of NLoS paths on LoS angular estimation, as well as the CRLB on 3D localisation, we design the following practical localisation scheme. By first resorting to the atomic norm minimisation (ANM) and subspace-based root MUSIC algorithms to estimate the angular parameters for the LoS path at each R-RIS subarray, we then apply the Least Squares principle to map the angular estimates to the 3D localisation of the Mobile Stations (MS).

Results and discussion

We first evaluate the performance of the proposed scheme in terms of the RMSE (in meters) as a function of the transmit power P, where different training overheads values are considered. In Figure 3-9, it is shown that, as expected, the higher the training overhead is, the better becomes the estimation performance. When the transmit power is equal to 20 dBm, ANM with $K = 64$ the accuracy is around 1 cm. Hence, based on the fact that LoS information can bring cm-level accuracy, there is no need to exploit NLoS path information, which would increase the computational complexity of the proposed algorithm. It is also illustrated that the performance of the introduced orthogonal matching pursuit (OMP) saturates to 7 cm as P increases due to inevitable quantisation error, since an extremely large dictionary has been used for the proposed algorithm, as detailed in [HFV+23]. Moreover, it is also depicted that the performance gap between the theoretical and practical results stays constant within the SNR range under investigation.

In Figure 3-10, different inter R-RIS subarray spacings are considered, in order to evaluate the impact on the 3D localisation accuracy. Assuming specific centroid coordinates of the whole R-RIS, and changing the vertical and horizontal distances of the R-RIS subarrays (as illustrated in the legend of the mentioned figure), it can be inferred that the case where $d_V = d_H = 1.2$, can achieve around 2 cm accuracy, while when $d_V = d_H = 0.2$ only 6 cm accuracy can be achieved.

Therefore, we can reach the conclusion that larger spacing in general can provide better performance, but at a sacrifice of a larger space for installing the overall R-RIS structure.
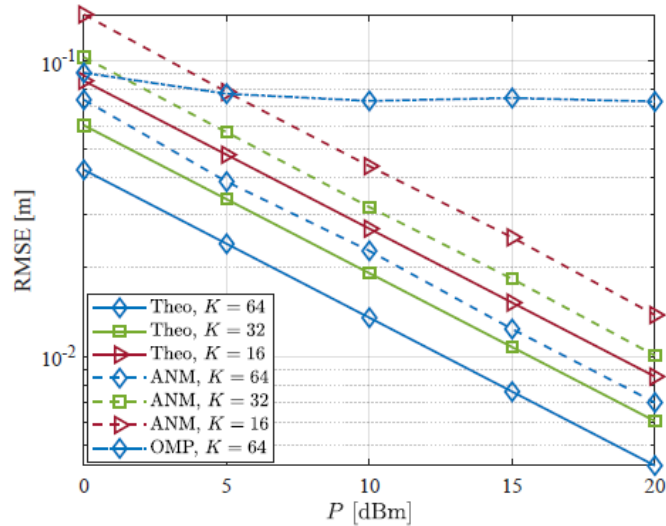
Figure 3-9. RMSE performance of the proposed 3D localisation system with different training overhead values.
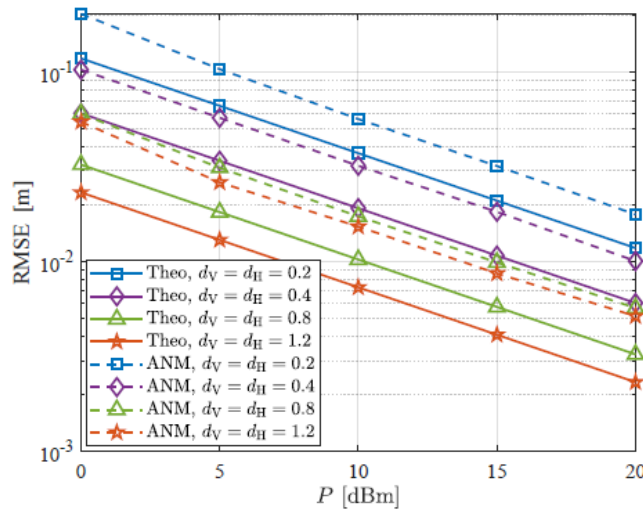
Figure 3-10. Effect of R-RIS partitioning on the RMSE performance from both the theoretical and practical perspectives.

Perspective and relation to other WP5 contributions

This contribution considers the algorithmic aspects of a minimal monostatic RIS localisation architecture, whose control and signalling have been discussed under contribution #C8 of D5.3 [RISED53]. The multiple RF chains endowed to the surface allow for typical sparse signal recovery and matching algorithms to be applied to decompose the LOS path, as normally done by other localisation contributions of this deliverable.

3.3 Set of contributions #B

Table 3-2 An overview of active UE location estimation contributions

Architecture	Cont. #B-1: Semi-passive Localisation of Multiple RIS Enabled Users	Cont. #B-2: RIS-Enabled SISO Localisation under User Mobility and Spatial-Wideband Effects	Cont. #B-3: RIS-Enabled Self-Localisation: Leveraging Controllable Reflections with Zero Access Points	Cont. #B-4: RIS-aided Near-Field Localisation under Phase-Dependent Amplitude Variations	Cont. #B-5: Localisation via multiple sensing reconfigurable intelligent surfaces, without any BSs
Nr BS	1	1	0	1	0
Nr RIS	Multiple	1	1	1	At least 2
Nr UEs	Multiple	1	1	1	1
UE Mobility	Stationary	Mobile	Stationary	Stationary	Stationary
RIS Type	Reflective	Reflective	Reflective	Reflective	Sensing
Localisation functionality placement	At Rx	At UE	At UE	At UE	At RIS
Setup					
Uplink/Downlink	DL	DL	UL	DL	UL
Indoor/outdoor/UAV	Outdoor	Outdoor	Outdoor	Indoor/outdoor	Indoor/outdoor
Frequency Band	30 GHz	28 GHz	28 GHz	28 GHz	30 GHz
Narrowband/wideband	Wideband	Wdeband	Wideband	NB	NB
Near field/far field	Far field	Far field	Far field	NF	Both
LOS/NLOS (BS-RIS-UE)	LOS (Tx-Rx) and NLOS (Tx-RIS-Rx)	LOS (BS-UE) and NLOS (BS-RIS-UE)	LOS (UE-RIS-UE)	NLOS	RIS- UE LOS/NLOS
Imperfections or other hardware considerations	-	-	-	Phase-dependent RIS amplitude variations	-
Measurement type	ToA and AoD	ToA and AoD	ToA and AoD	ToA and AoD	AoA
RIS configuration strategy	Random	Directional	Directional	Random	Random or DFT
Who collects measurements	Rx	UE	UE	UE	RIS
Synchronisation	Unsynchronized	Unsynchronized	No	No	No
Metric optimised	No optimization	No optimization	No optimization	No optimization	No optimization

Architecture	Cont. #B-6: RIS-Enabled Joint Mobile User Location and Velocity Estimation in Near-Field	Cont. #B-7: RIS-aided Localization under Pixel Failures	Cont. #B-8: Joint RIS Calibration and User Positioning	Cont. #B-9: Multi-RIS-Enabled 3D Sidelink Positioning
Nr BS	1	1	1	0
Nr RIS	1	1	1	Multiple
Nr UEs	1	1	1	Multiple
UE Mobility	mobile	Stationary	Stationary	Stationary
RIS Type	reflective	Reflective	Active	Reflective
Localisation functionality placement	At UE	At UE	At BS	At UE
Setup				
Uplink/Downlink	DL	DL	UL	DL
Indoor/outdoor/UAV	Indoor/outdoor	Indoor/Outdoor	Outdoor/UAV	Outdoor
Frequency Band	28 GHz or sub-6 GHz	28 GHz	28 GHz	28 GHz

Narrow-band/wide-band	NB	NB	WB	WB
Near field/far field	NF	NF	FF	FF
LOS/NLOS (BS-RIS-UE)	NLOS	NLOS (BS-RIS-UE)	LOS and NLOS	LOS (TxUE-RxUE) and NLOS (TxUE-RIS-RxUE)
Imperfections or other hardware considerations	Single antenna BS and UE	Pixel failures at RIS	-	-
Measurement type	ToA, AoD, channel gain, velocity (intermediary/approximate)	Wavefront curvature	ToA, AoA, Spatial frequency	AoD, AoA, Spatial frequency
RIS configuration strategy	Random, directional and extended to optimal	Random	Random	Random, directional, and derivative codebook
Who collects measurements	BS	UE	BS	UE
Synchronisation	unsynchronized	Unsynchronized	Unsynchronized	Unsynchronized
Metric optimised	No optimization	No optimization	No optimization	No optimization

#B-1: Semi-passive localisation of multiple RIS enabled users

Please refer to D5.2 [RISED52] for an extended description of this contribution.

#B-2: RIS-enabled SISO localisation under user mobility and spatial-wideband effects

Please refer to D5.2 [RISED52] for an extended description of this contribution.

#B-3: RIS-enabled self-localisation: leveraging controllable reflections with zero access points

Please refer to D5.2 [RISED52] for an extended description of this contribution.

#B-4: RIS-aided near-field localisation under phase-dependent amplitude variations

Please refer to D5.2 [RISED52] for an extended description of this contribution.

#B-5: Localisation via multiple sensing reconfigurable intelligent surfaces, without any BSs

Please refer to D5.2 [RISED52] for an extended description of this contribution.

#B-6: RIS-enabled joint mobile user location and velocity estimation in near-field

Motivation and context

In this contribution, the position and velocity of a single-antenna UE are jointly estimated (i.e., performing 6D state estimation) out of DL narrowband pilot transmissions from a single-antenna BS, while still the direct path between the BS and UE is blocked (i.e., assuming NLoS). Just like in contribution #A-5, the main idea is to benefit from the small-scale Doppler effects induced by mobility at the multiple elements of a large reflective RIS in the NF propagation regime. In this scenario again, localisation is made feasible by the RIS-reflected path assuming NF propagation, just like in [RDK+21]. To some extent, this approach can hence be seen as a dual –yet

extended or generalized- variant of the position-based velocity estimation approach described above in #A-5. Regarding this new joint position and estimation problem, both the analytical position error bound (PEB) and velocity error bound (VEB) were initially derived in [RISED52] for benchmark purposes.

Figure 3-11. Considered scenario and problem geometry for RIS-aided joint user position and velocity estimation over DL pilots transmission in NF NLoS conditions.

Methodology

A practical initialization procedure based on 2 simple grid searches (GS), over the RIS AoD and BS-RIS-UE range domains for a simplified closed-form channel gain model was first proposed. This initialisation provides coarse estimates for both the 3D UE position and the complex channel gain of the RIS-reflected path, while relying on static UE assumption and FF approximation. The corresponding results are then injected into a generic and complete NF RIS response formulation for further corrections, while still assuming a null velocity. Then, a closed-form (CF) refinement algorithm fed by the previous initialization steps is applied, which iterates alternatively over both position-based velocity estimate and velocity-based position estimate, while performing local linearization steps and compensating for the estimation residuals caused by mobility at each iteration.

Finally, an optional Quasi-Newton refinement routine is performed to complete the estimation process and further improve position, velocity and channel gain estimates through standard Likelihood maximization. This extra refinement step can be activated or inhibited on demand, typically depending on the RIS-UE distance, as its actual gain (beyond the previous algorithmic step) depends on the experienced FF/NF regime.

Results and discussion

Just like for #A-5, the performance of the proposed joint estimation approach was evaluated through simulations and compared with the two theoretical bounds from [RISED52], as well as with other algorithmic variants assuming for instance NF but no velocity at all, while also illustrating the impact of the actual RIS-UE distance or velocity module.

First, in Figure 3-12, we plot the PEB of our problem to assess the feasibility and the performance bound on any estimator we would design. Then, the output of our iterative GS routine is plotted in solid red. We could see that it is not attaining the PEB neither at NF nor at FF, although at short distances it performs worse. This is due to the mismatch caused by the FF approximation that we try to overcome with the iterative nature of this routine. Clearly, the output of this

algorithm is still far from optimal and needs to be refined, but nevertheless we compare it with the method proposed in State of the Art [ZKM+21] in NLoS NF scenarios. The latter applies a non-iterative GS algorithm that does three 1D searches, i.e., two angular and one range, in contrast to our method which applies a 2D angular search (with FF assumption) and then iterates over a linear search to get the range and again the 2D angular search to overcome the NF-FF mismatch. In comparison, the State of the Art method, with its simplicity, is then shown to fail to a larger extent when the UE is mobile.
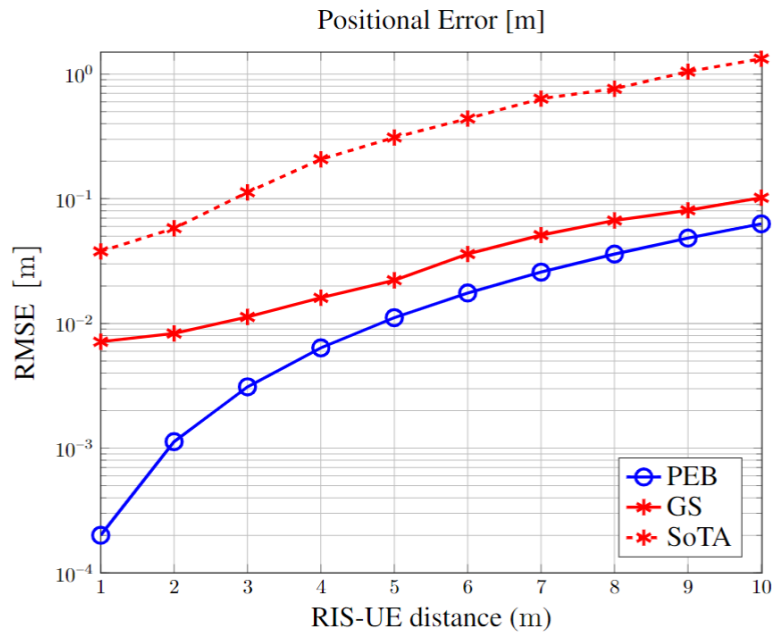

Figure 3-12. UE's position estimation error versus RIS-UE distance, with the proposed initial grid search step, against the State of the Art algorithm [ZKM+21], for v = 1 m/s.
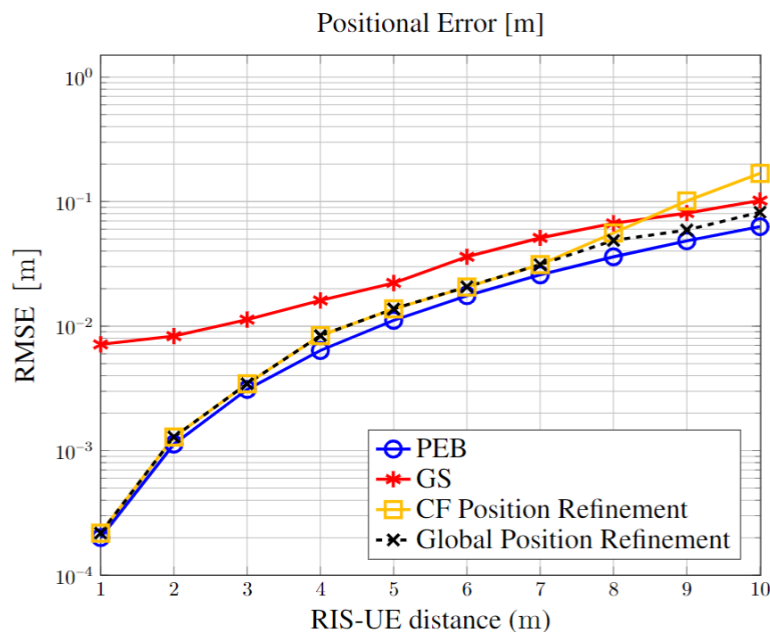

Figure 3-13. UE's position estimation error versus RIS-UE distance, with the overall algorithm proposal (full model), for v = 1m/s.

Next, we have implemented our CF velocity-based position refinement routine, which was derived by linearising the position component in the RIS response phase term and then by performing a small angle approximation (SAA). This routine is fed with the output of the GS algorithm (in red) and already, in Figure 3-13, we see a significant improvement (in amber) in the estimation algorithm, at least at short distance where the performance touches the PEB. However, as the UE is moving away from the RIS, we start noticing performance degradation of this algorithm, which is an aftermath of the linearization/approximation steps that were needed to develop this algorithm.
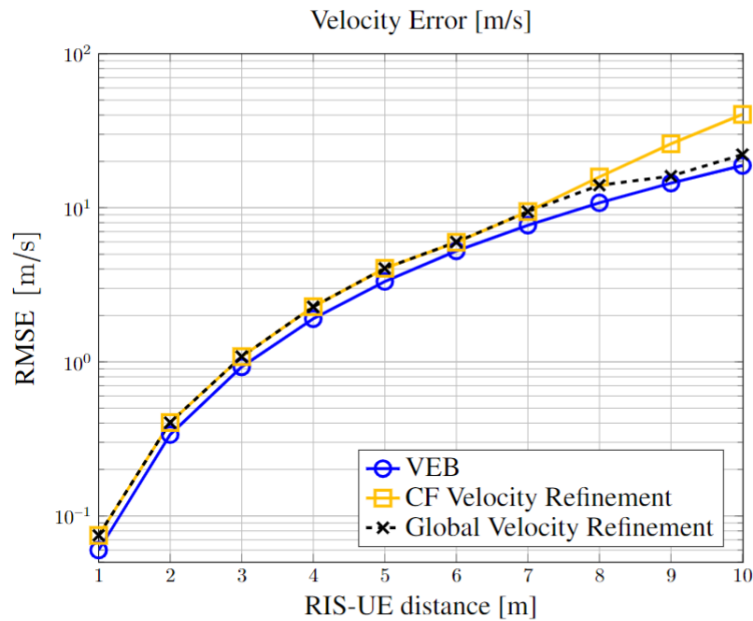

Figure 3-14. UE's velocity estimation error versus RIS-UE distance, with the overall algorithm proposal (full model), for v = 1m/s.

Additionally, and as a part of the 6D estimation system, we have plotted in Figure 3-14 the VEB (in blue) which acts as the bound for any unbiased velocity estimator alongside the latter (in amber) and a global velocity refinement routine (in black - dashed). Our estimator is still labelled as "refinement" here because we start the estimation from zero velocity assumption and position estimate gained from amber curve in Figure 3-13 and the iteration between both starts until our objective function converges. We can see similar performance to the velocity-based position estimation algorithm, the estimator being very close to the theoretical bound, i.e., VEB, until far distances where the global refinement routine fixes the issue.

Perspective and relation to other WP5 contributions

The proposed approach can be combined with both Bayesian filtering (i.e., feeding the filter with the previous snapshot position and velocity estimates, as observations) and dynamic RIS control, thus benefiting from the filtered 6D state estimates (along with their associated estimation covariance) to anticipate on the best localisation-optimal RIS configuration at any place and time through robust phase design.

#B-7: RIS-aided localization under pixel failures

Motivation and context

Certain aspects warrant careful consideration when dealing with practical RISs, which may encompass numerous unit elements (or pixels). Among these concerns is the potential occurrence of individual element failures, a topic that has also been explored in the array processing literature. In a standard mmWave setup without an RIS, researchers have studied antenna array

diagnosis in [EAH18], where several compressive sensing-based techniques have been proposed to detect faulty antenna elements and analyse the resulting amplitude and phase distortions. Moreover, AoA estimation under element failures has been addressed in [SWS+19].

Recent investigations have focused on RIS element failures in mmWave communications [TCG+20], [SWC+22], [ZHZ22]. In [TCG+20], the authors identified various types of pixel errors (e.g., stuck at state, out of state, etc.) and assessed their spatial distribution (independent, clustered, etc.) along with their impact on the radiation pattern through simulation analysis. Similarly, in [SWC+22], a failure model was established to define the amplitude and phase shift of faulty elements, and they proposed diagnostic methods exploiting the sparsity property of these failures. Despite substantial research on pixel failures in RIS-aided communications, no study has yet addressed the problem of RIS-aided localisation in the presence of pixel failures. This work investigates the impact of RIS pixel failures on localisation accuracy in a near-field SISO scenario under LoS blockage and proposes two sparsity-inspired algorithms for joint localisation and failure diagnosis (JLFD) to simultaneously estimate user location and detect failing RIS elements.

Methodology

To model RIS pixel failures, the biased failure model is adopted, where applied RIS phase shifts are perturbed by unknown phases and amplitudes (less than 1) in failing elements. Considering a near-field SISO downlink scenario under LoS blockage between the BS and the UE, a single path (i.e., BS-RIS-UE) is assumed to exist without any uncontrolled multipath. The goal is to estimate the UE location while simultaneously detecting pixel failures and estimating the respective failure coefficients (i.e., the failure mask). For this problem, the methodology consists of two stages:

- *Localisation performance evaluation in the presence of pixel failures:* We first evaluate how severe the effect of RIS pixel failures can be on localisation accuracy when the UE is unaware of these failures. To this end, we resort to the Miss-specified Cramer Rao Bound (MCRB) analysis as a theoretical tool to assess degradation accuracy due to mismatch between the true model with failures and the ideal model without failures. The MCRB serves as a fundamental theoretical benchmark for evaluating the performance limits of conventional localisation algorithms when facing pixel failures.

- *Development of JLFD algorithms to mitigate the impact of failures:* Exploiting the sparsity of failures, two novel algorithms are proposed to solve the JLFD problem:

  - The JLFD problem is formulated using the hybrid Maximum Likelihood/Maximum A Posteriori (ML/MAP) estimation framework, where the UE location is a deterministic unknown, and the failure mask is a random unknown parameter with certain statistical distribution (each pixel fails independently with the same failure probability).

  - Due to binary failing/functioning variables for each pixel, the resulting optimization problem has a combinatorial nature, leading to a computationally intractable problem.

  - To tackle this challenge, an l-1 regularization based JLFD algorithm (called l1-JLFD) is proposed, and an alternating minimization strategy is developed to update failure mask and UE location in an alternating manner.

  - In addition, we propose a successive-JLFD algorithm that solves the hybrid ML/MAP optimization problem in an iterative fashion. The successive-JLFD detects pixel failures one-by-one per iteration and estimates the corresponding failure coefficient while at the same time updating the UE location estimate.

Results and discussion

We investigate the localisation performance under pixel failures by plotting standard CRLB (which assumes known failure mask) and another Lower Bound (LB) (obtained from MCRB analysis, which provides a lower bound on accuracy when failures are ignored in receiver processing). Figure 3-15 shows the localisation RMSE with respect to failure probability and SNR. By comparing LB and CRLB curves, it is observed that the gap between LB and CRLB gets larger with increasing failure probability due to increasing mismatch between the true and ideal models. We see that severe degradations in accuracy can occur, especially at high SNRs and for large probability of failures (greater than 1%), when the UE performs conventional processing by ignoring the existence of failures. Therefore, RIS-aided localisation can be highly sensitive to pixel failures. This mainly results from the fact that localisation in the considered SISO scenario with LoS blockage relies purely on location-dependent phase shifts across the RIS, which, however, are impaired by unknown complex failure coefficients in failing pixels.
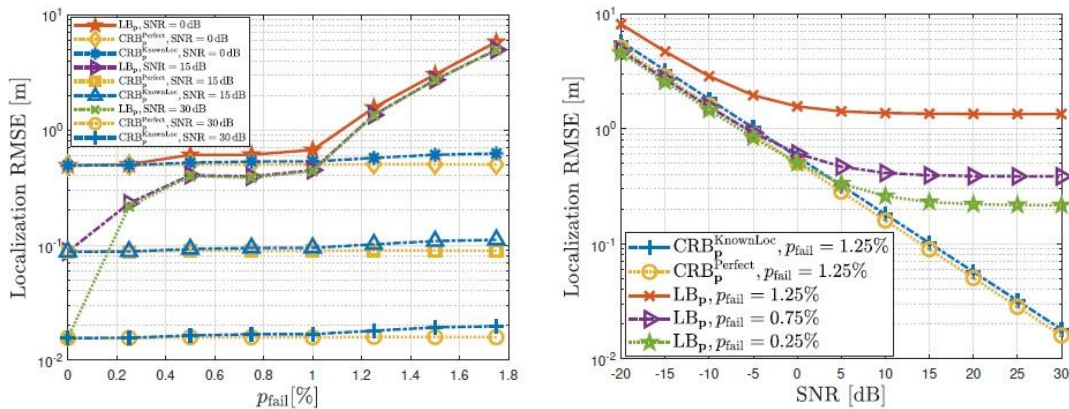

Figure 3-15. Theoretical limits on localisation RMSE under pixel failures with respect to failure probability and SNR.

We also explore the performance of the proposed JLFD algorithms along with a failure-agnostic benchmark method which performs standard ML location estimation without taking into account the presence of failures. Figure 3-16 shows the RMSE results with respect to SNR for two different values of probability of failure. It is observed that the benchmark reaches a plateau in localisation performance after a certain SNR, attaining its respective bound (LB), while the successive-JLFD algorithm can successfully recover failure-induced performance losses and achieve the corresponding CRLB (which has the knowledge of failure mask). By fully exploiting the failure statistics, the successive-JLFD algorithm outperforms both the l1-JLFD and the benchmark, especially for high percentage of failures. The l1-JLFD exploits only the sparsity property of failures without using the full statistics, leading to a computationally cheaper but less accurate method than the successive–JLFD.
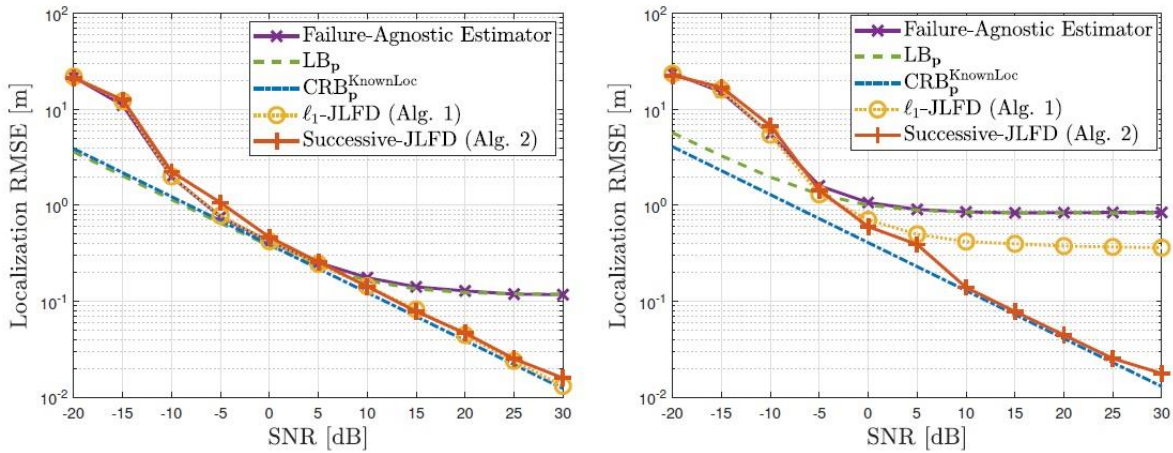

Figure 3-16. Localisation RMSEs achieved by the proposed algorithms and the failure-agnostic estimator, along with the theoretical limits, with respect to SNR for probability of failure 0.5% (left) and 1% (right).

Finally, we provide an illustrative example on failure mask estimates obtained by the proposed algorithms in Figure 3-17. It is seen that the successive-JLFD accurately detects the locations of failing elements and estimates the respective coefficients while the l1-JLFD fails to detect the location of one failure and suffers from high errors in coefficient estimation.
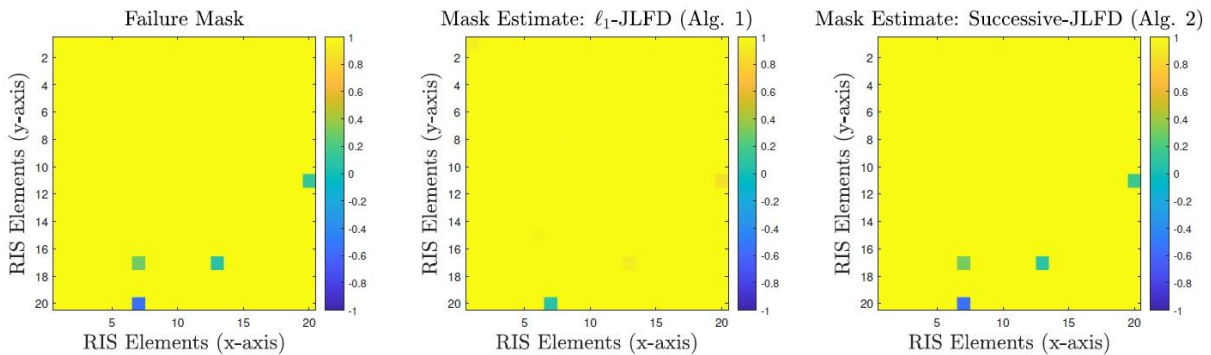
Figure 3-17. Failure mask and its estimates by the proposed algorithms.

Perspective and relation to other WP5 contributions

We have analysed the performance of RIS-aided localisation in NLoS scenarios under RIS pixel failures and demonstrated high sensitivity of localisation to failing elements especially at high SNRs and for large percentage of failures. The effectiveness of the algorithms has been corroborated through simulations under different settings regarding SNR and failure probability showing a huge impact on other WP5 contributions, where RISs are considered as fully-working devices.

#B-8: Joint RIS calibration and user positioning

Motivation and context

As described in #A-6, RIS calibration is a crucial step before providing RIS-aided localisation and sensing service, and a novel JrCUP algorithm is proposed to tackle this issue practically. The three-dimensional (3D) JrCUP localisation problem was first formulated in [LCT+22], which

explored the relationship between the channel parameters and localisation unknowns, with the corresponding Fisher information matrix derived and analysed. Nonetheless, the adopted passive RIS in [LCT+22] limits the localisation performance, and the design of an efficient channel estimator for JrCUP is still missing. In [GCA+22], a multi-stage solution for the two-dimensional (2D) JrCUP problem in a hybrid RIS-assisted system is reported. However, the hybrid RIS setup requires an extra central processing unit (CPU) for the receiver and RIS to share observations, which increases the system complexity. In this work, we extend the 3D JrCUP problem in [LCT+22] and utilizing active RISs to improve localisation performance. Based on the estimated channel parameters $\boldsymbol{\theta}_\mathrm{L}$, $\boldsymbol{\theta}_\mathrm{R}$, τ_L, τ_R, and $\boldsymbol{\vartheta}$, we develop JrCUP algorithms to obtain the 3D positions of UE, RIS, 1D orientation of the RIS, and the clock offset ($\mathbf{p}_\mathrm{U}$, $\mathbf{p}_\mathrm{R}$, o_3, and Δ).

Methodology

Based on the refined channel parameters estimates, the localisation parameters can be recovered by carrying out a 2D search over o_3, and Δ; the rest of the localisation parameters can be determined from each search point $[o_3, \Delta]$ and a cost metric can be defined to compare the fitness of different search points. More specifically, for each candidate search point $[\check{o}_3, \check{\Delta}]$, candidate distances of the LoS path and RIS reflected path can be obtained by the subtraction of delay and clock offset and convert to meter. Then, the UE position candidate $\check{\mathbf{p}}_\mathrm{U}$ can be obtained via the LoS AoA at the BS, and the RIS position $\check{\mathbf{p}}_\mathrm{R}$ can be obtained as the intersection of the ellipsoid and the line formulated by distance candidates. Then, the cost metric can be computed based on the predicted intermediate measurements ($\check{\vartheta}_2, \check{\vartheta}_3$) and the estimated ones ($\hat{\vartheta}_2, \hat{\vartheta}_2$) as follows

$$f\left(\check{o}_3, \check{\Delta}\right) = \left\|\left[\check{\vartheta}_2, \check{\vartheta}_3\right]^\mathrm{T} - \left[\hat{\vartheta}_2, \hat{\vartheta}_2\right]^\mathrm{T}\right\|_2^2.$$

The search point that minimizes the cost metric is chosen as the estimates of ($\hat{o}_3, \check{\Delta}$), which will be used to compute other state parameters. Multiple iterations of search grid refinement can be performed to obtain more accurate estimations.

Results and discussion

We assess the performance for the localisation parameters estimation. Figure 3-18 presents the RMSEs of estimating $\mathbf{p}_\mathrm{U}$, $\mathbf{p}_\mathrm{R}$, and o_3 versus the received SNR for different numbers (0,1,2,3) of grid-search refinement iterations. It can be observed that in the low SNR regions (lower than 10 dB), the RMSEs stay far from the theoretical bound. In these regimes, increasing the number of grid-search refinements does not improve performance. In the high SNR regions (10dB or higher), however, we can see that the RMSEs decrease as more search refinements are carried out. The RMSEs follow the CRLB closely after two or more search iterations are performed. These results confirm that our proposed algorithms can achieve a nearly efficient localisation performance at practical SNRs (higher than 10dB). Finally, the refinement dependence of performance presents an unavoidable trade-off between localisation accuracy and computational complexity in practice.
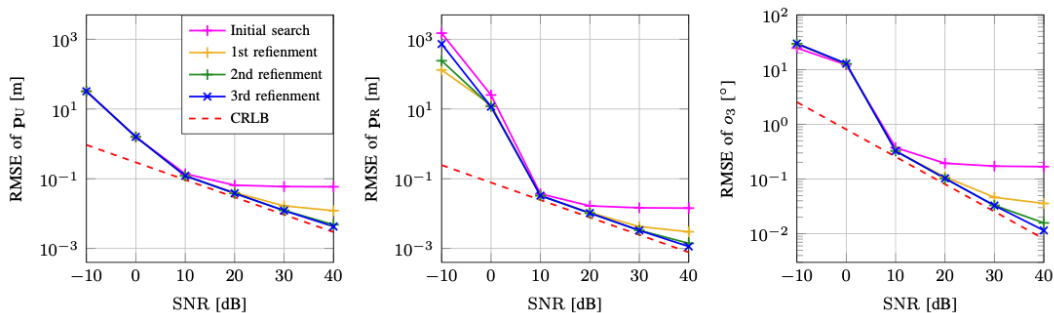

Figure 3-18. The evaluation of RMSE of state parameters versus received SNR for different numbers (0, 1, 2, 3) of grid-search refinements.

We also examine the spatial variability of performance. To this end, we consider three different scenarios, i.e., the base scenario, changing the BS position, and changing the RIS orientation. The error bounds of $\mathbf{p}_U$, $\mathbf{p}_R$, and o_3 are computed over different UE positions while the BS and RIS positions and orientations are kept fixed. We assume the UE to be placed across at 10mx10m space at a fixed height (1m by default). Figure 3-19 shows the presence of areas with extremely high CRLB (yellow areas), with a noticeable variability in the patterns across the different setups. Since these areas with high CRLB yield a poor localisation performance or are even unable to perform localisation, which are named as blind areas.
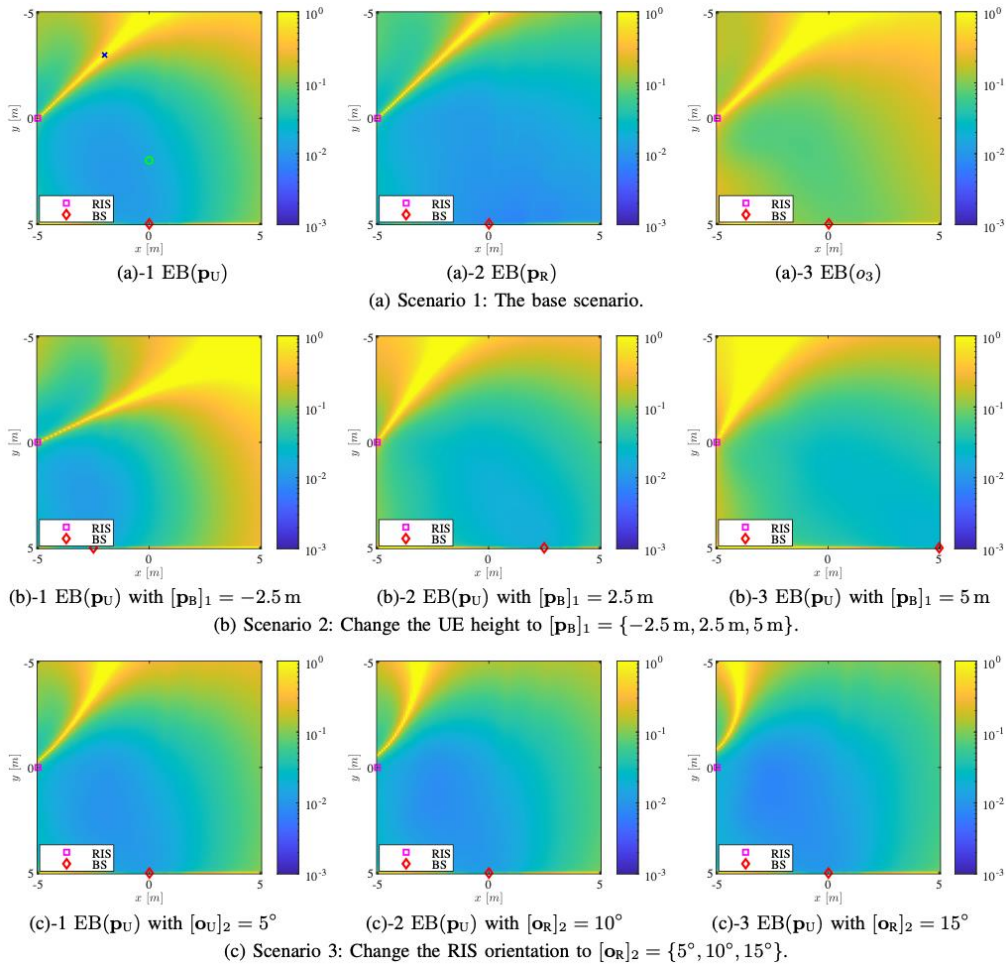

(a)-1 EB($\mathbf{p}_U$)   (a)-2 EB($\mathbf{p}_R$)   (a)-3 EB(o_3)

(a) Scenario 1: The base scenario.

(b)-1 EB($\mathbf{p}_U$) with $[\mathbf{p}_B]_1 = -2.5\,\mathrm{m}$ (b)-2 EB($\mathbf{p}_U$) with $[\mathbf{p}_B]_1 = 2.5\,\mathrm{m}$ (b)-3 EB($\mathbf{p}_U$) with $[\mathbf{p}_B]_1 = 5\,\mathrm{m}$

(b) Scenario 2: Change the UE height to $[\mathbf{p}_B]_1 = \{-2.5\,\mathrm{m}, 2.5\,\mathrm{m}, 5\,\mathrm{m}\}$.

(c)-1 EB($\mathbf{p}_U$) with $[\mathbf{o}_U]_2 = 5°$ (c)-2 EB($\mathbf{p}_U$) with $[\mathbf{o}_R]_2 = 10°$ (c)-3 EB($\mathbf{p}_U$) with $[\mathbf{o}_R]_2 = 15°$

(c) Scenario 3: Change the RIS orientation to $[\mathbf{o}_R]_2 = \{5°, 10°, 15°\}$.

Figure 3-19. Visualization of blind areas under different scenarios.

Perspective and relation to other WP5 contributions

We have detailed the grid search-based JrCUP algorithm given the estimated channel parameters. The simulation results validate the effectiveness of the proposed algorithm, and we should be aware of the blind areas while performing JrCUP tasks.

#B-9: Multi-RIS-enabled 3D sidelink positioning

Motivation and context

The discussion on combining sidelink communication and RIS for low-latency and high-reliability communication has been discussed in [GZJ+22], while positioning works appear quite recently [CKA+23], [BGV+22] with a major feature of no BSs being involved, resulting in the Tx and Rx, both with unknown positions. In [CKA+23], sidelink positioning with RISs is discussed at a high level with localisation and sensing scenarios, architectures, and protocols being discussed. The work in [BGV+22] requires the cooperation of multiple UEs and RISs with different states (e.g., enabled or disabled), and only time-of-arrival information is considered without benefiting from the high angular resolution of RISs. Self-localisation has been studied in [KCK+22] where the UE is equipped with a full-duplex array, introducing extra hardware cost. In this work, we will show that with a sufficient number of RISs (at least two) involved, the 3D absolute positions of two single-antenna UEs can be estimated using sidelink communication in the absence of BSs, making ubiquitous positioning possible. In this work, we consider a 3D SISO sidelink communication scenario with two UEs and several passive RIS anchors.

Methodology

Based on the estimated channel parameters, namely, delay of the LoS path (d_0), delay and spatial frequency of all the RIS paths (e.g., d_ℓ, ξ_ℓ, ζ_ℓ for the ℓth path), we propose a 3D-search positioning algorithm to estimate state unknowns (i.e., position of the transmitter $\mathbf{p}_T$, position of the receiver $\mathbf{p}_R$, and clock offset B). For each candidate transmitter position $\breve{\mathbf{p}}_T$, a candidate direction vector $\check{\mathbf{t}}_{R,\ell}$ from the ℓth RIS to the Rx can be obtained [CZK+23]. Since the RIS states are known, we are able to calculate the candidate receiver UE position $\breve{\mathbf{p}}_R$ by getting the closest point to all the AOD direction vector candidates [BAS97]. Then, the estimated clock offset $\breve{B}$ can be obtained as $\breve{B} = c\hat{\tau}_0 - \|\breve{\mathbf{p}}_T - \breve{\mathbf{p}}_R\|$, and the cost function can be formulated as

$$J(\breve{\mathbf{p}}_T) = \sum_{\ell=1}^{L} w_\ell \, |\breve{B} + \|\breve{\mathbf{p}}_T - \breve{\mathbf{p}}_\ell\| + \|\breve{\mathbf{p}}_\ell - \breve{\mathbf{p}}_R\| - c\hat{\tau}_\ell|,$$

With w_ℓ as the weighting coefficients. Among all the transmitter UE position candidates, the one with the lowest cost will be the estimated position and the rest of the state parameter vector can be obtained accordingly. From the estimated state vectors, a maximum likelihood estimator (MLE) can be formulated to further refine the localisation results.

Results and discussion

The positioning results are shown in Figure 3-20. Similar to the channel estimation results, the refinement processes can improve the coarse estimation and attach the derived CRB.
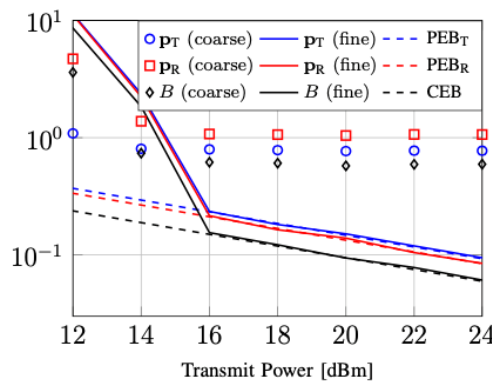

Figure 3-20. Positioning accuracy for different transmit power values.

We further explore the effect of multipath on sidelink positioning by creating two clusters of SPs. More details can be found in [CZK+23]. We can see that different SPs properties (e.g.,

reflection coefficient, positions) affect positioning performance differently, and large transmit power could help to combat the multipath.
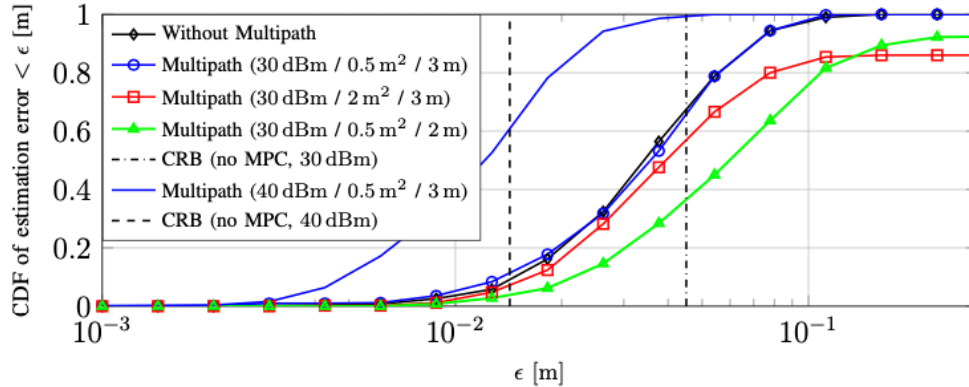

Figure 3-21. Evaluation of the multipath on the estimator.

We also evaluated the effect of the number of RISs on positioning with four anchors, and the PEBs heatmap of a RX moving within an 8mx8m area are shown in Figure 3-22. In general, more RISs can increase positioning coverage; however, if the same orthogonal strategy is implemented, more blocks are needed, increasing difficulties in coordinating between these RISs and channel parameter estimation.
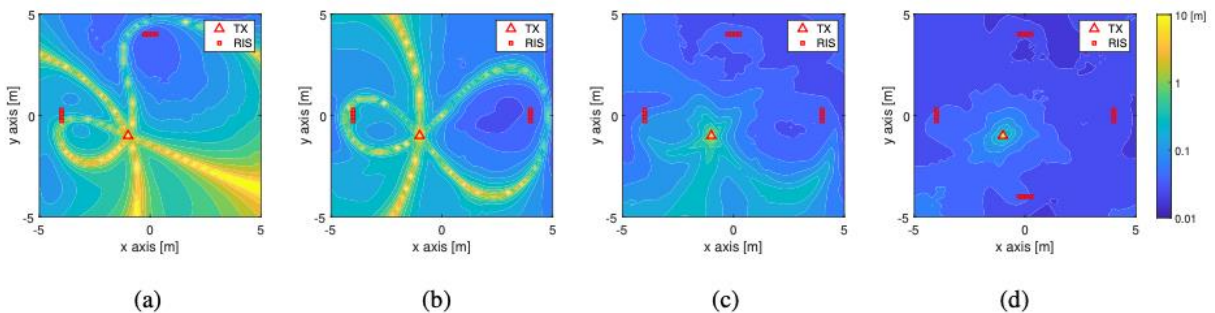

Figure 3-22. Visualization of RX PEBs for different numbers of RISs.

Perspective and relation to other WP5 contributions

We have formulated and solved the multi-RIS-enabled 3D sidelink positioning problem. In this problem, with the assistance of at least two RISs, the absolute positions of two unsynchronized UEs can be estimated via a one-way sidelink communication in the absence of BSs. We discussed the effect of multipath on positioning performance and evaluated the performance improvement with more RISs. However, this work is just the starting point for sidelink positioning with simplified scenarios and channel models.

3.4 Set of contributions #C

Table 3-3 An overview of SLAM and passive object detection contributions

Architecture	Cont. #C-1: RIS-Enabled Self-lo-calisation and	Cont. #C-2: Assessing Wire-less Sensing Potential With	Cont. #C-3: Radio Sensing	Cont. #C-4: AI-based intrusion detection using	*Cont. #C-5: RIS-enabled sensing with single- and*

	SLAM with Zero Access Points	Large Intelligent Surfaces	with Large Intelligent Surface for 6G	Intelligent Surfaces at mmWave	*double bounce signals*
Nr BS	0	0	0	1 or more	0
Nr RIS	1	1	1	Multiple	1
Nr UEs	1	Single	Multiple	Multiple	1
UE Mobility	Moving	Moving	Moving	Fixed	Fixed
RIS Type	Reflective	Receiving	Receiving	Reflective	Reflective
Localisation functionality placement	At UE	At RIS	at RIS	At BS	At UE
Setup					
Uplink/Downlink	UL	UL	UL	UL/DL	UL
Indoor/outdoor/UAV	Outdoor	Indoor	Indoor	Indoor	Outdoor/Indoor
Frequency Band	30 GHz	Sub-6 GHz	Sub-6 GHz	60-GHz	28 GHz
Narrowband/wideband	Wideband	narrowband	narrowband	narrowband	Wideband
Near field/far field	Far field	Near-field	Near-field	Far-field	Far field
LOS/NLOS (BS-RIS-UE)	LOS (UE-RIS-UE) and NLOS (UE-landmark-UE)	LOS and NLOS	LOS	LOS and NLOS	LOS (UE-RIS-UE) and NLOS (UE-RIS-landmark-UE, UE-landmark,RIS-UE, and UE-landmark-UE)
Imperfections or other hardware considerations	-	-	-	Imperfect beam patterns	-
Measurement type	ToA and AoD	RSS at RIS	Complex signal	RSS at BS and UEs	TOA, AOD, and AOA
RIS configuration strategy	Arbitrary	Arbitrary	Arbitrary	Beam sweep	Random
Who collects measurements	UE	RIS	RIS	BS and UEs	UE

#C-1: RIS-enabled self-localisation and SLAM with zero access points

Please refer to D5.2 [RISED52] for an extended description of this contribution.

#C-2: Assessing wireless sensing potential with large intelligent surfaces

Please refer to D5.2 [RISED52] for an extended description of this contribution.

#C-3: Radio sensing with large intelligent surface for 6G

Please refer to D5.2 [RISED52] for an extended description of this contribution.

#C-4: AI-based intrusion detection using Intelligent Surfaces at mmWave

Please refer to D5.2 [RISED52] for an extended description of this contribution.

#C-5: RIS-enabled sensing with single- and double-bounce signals

Motivation and context

In this work, the separation of the single- and double-bounce signals is studied in the context of monostatic sensing [KFC+22]. A full-duplex UE transmits a signal using an antenna array and receives the back-propagated signals. As shown in Figure 3-23, the four different types of paths are considered: two single-bounce paths, UE-RIS-UE (shown in blue) and UE-SP-UE (shown in red). There are also two double-bounce paths per SP, UE-RIS-SP-UE (shown in black) and UE-SP-RIS-UE (shown in green). Higher-order bounces that are more than two are ignored since they are much weaker than single- and double-bounce signals. The signal paths i) UE-RIS-UE, ii) UE-RIS-SP-UE, iii) UE-SP-RIS-UE can be controlled by the RIS while those in iv) UE-SP-UE cannot. The signal paths are separated and analysed, and the SP locations are estimated.
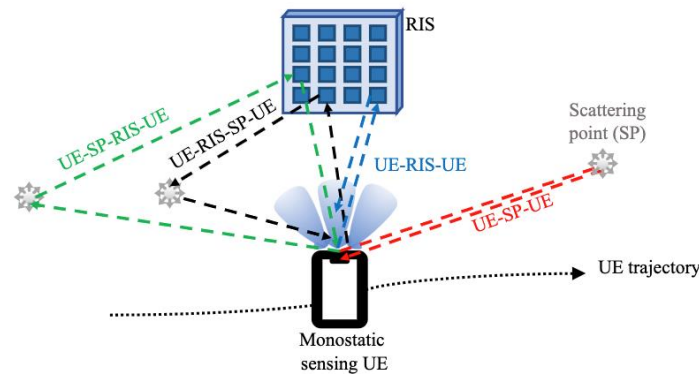

Figure 3-23. The considered sensing scenario, where a monostatic sensing UE receives the different four types of signal paths.

Methodology

By adopting the orthogonal RIS codebook design [KSA+22], the received signal is divided into controlled and uncontrolled path. The uncontrolled path corresponds to iv) UE-SP-UE, and the precoder is designed for the separation of the controlled path. With the directional transmission to the RIS, ii) UE-RIS-SP-UE could be observable, and with the transmission with null to the RIS iii) UE-SP-RIS-UE could be obtained. The detection probabilities for signal paths are studied with hypothetical statistics [WS20]. Since each SP generates single- and double-bounce signals, the data association is handled by running the two Poisson-Multi-Bernoulli (PMB) filters.

Results and discussion

Figure 3-24 shows the complementary cumulative distribution function (CCDF) of detection probabilities for all combinations of different SPs locations and UE trajectories. Detection probabilities for the double-bounce signals are lower than that of UE-SP-UE, due to the severe path loss at the RIS reflection.
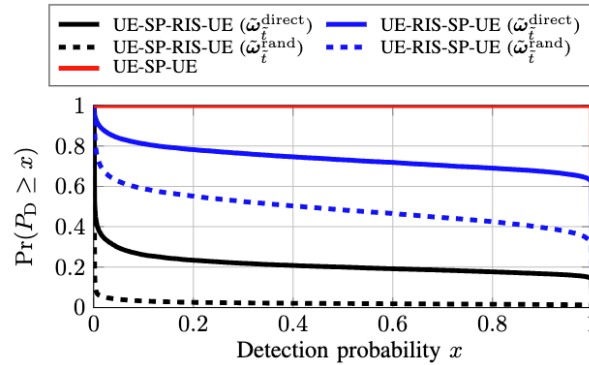
Figure 3-24. Detection probabilities for the different signal paths.

Figure 3-25 shows the sensing performance, evaluated by the Generalized Optimal Sub-pattern Assignment (GOSPA) distance. The SP GOSPA distances gradually decrease as the number of observable SPs via double-bounce signals increases over time steps while the SPs via the UE-SP-UE are always observable. In addition, the measurement noise covariances of the double-bounce signals are higher than the UE-SP-UE signal, due to the severe path loss. Therefore, the RIS-sensing performance is worse than the non RIS-sensing.
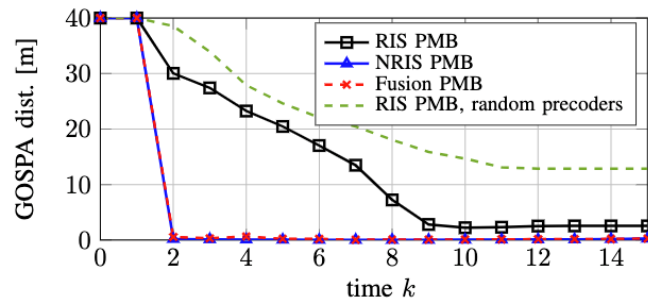

Figure 3-25. Sensing performance, evaluated by the GOSPA distance.

Figure 3-26 shows path losses for the different signal paths. In (a) and (b), the path UE-RIS-UE is generally stronger than the double-bounce paths, leading to severe interference (which was mitigated in this work by UE beamforming and combining). In scenario (b), the curves for UE-SP-UE and UE-RIS-SP-UE are the same as in scenario (a), due to the symmetry of the path loss. The difference lies in the UE-RIS-UE path, which is stronger when the UE is close to the RIS, but again nearly always dominates and thus interferes with the double-bounce paths.
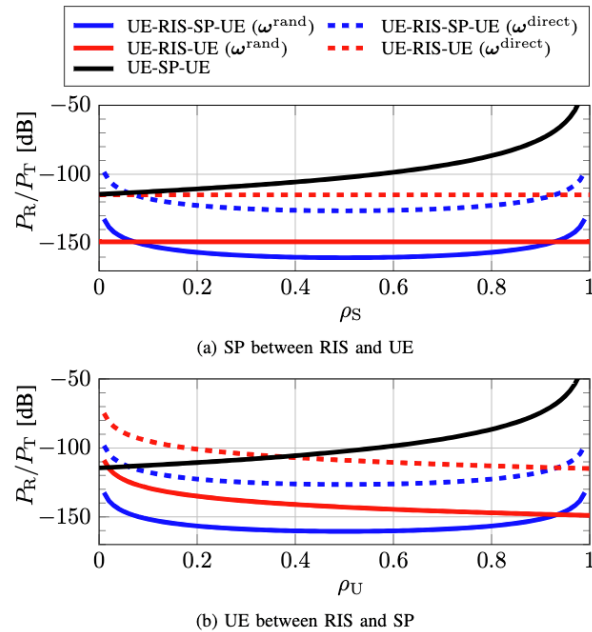
Figure 3-26. Path losses for the different signal paths.

Perspective and relation to other WP5 contributions

In this work that is extended from #C1, the double-bounce signals are additionally considered, which fundamentally makes sensing even more challenging. To facilitate signal separation, the precoder and combiner are designed. The detection probabilities for the separated signals are studied. The proposed methods could be used for multi-hypothesis testing in experimental positioning validations (See e.g., Section 4.1.2).

3.5 Set of contributions #D

Table 3-4 An overview of spectrum sensing, RF mapping and fingerprinting contributions

Architecture	Cont. #D-1: Graph-based Radio MAP Cartography for RIS-aided Fingerprinting Localisation	Cont. #D-2: OnRMap: An Online Radio Mapping Approach for Large Intelligent Surfaces	Cont. #D-3: RIS-Aided Wireless Fingerprinting Localisation based on Multilayer Graph Representations	Cont. #D-4: Practical AI-assisted RIS Planning
Nr BS	Multiple	N/A	Multiple	Multiple
Nr RIS	Multiple	Single	Multiple	Multiple
Nr UEs	1	Multiple	1	Multiple
UE Mobility	Static	Static	Static	Static
RIS Type	reflective / quasi-active	active	reflective / quasi-active	reflective
Setup				
Uplink/Downlink	DL	UL	DL	DL
Indoor/outdoor/UAV	Indoor/outdoor	Indoor	Indoor/outdoor	Indoor
Frequency Band	Any	Sub-6 GHz	Any	Any
Narrowband/wideband	NB	NB	NB	NB
Near field/far field	Far field	Near Field	Far field	Near/Far field
LOS/NLOS (BS-RIS-UE)	LOS/NLOS	LOS for RIS-UEs link/ NLOS for RIS-scatteres-UEs	LOS/NLOS	LOS/NLOS
Measurement type	Multiple RSSI	Multiple RSSI	Multiple RSSI	Multiple RSSI
RIS configuration strategy	Fixed set of sounding RIS profiles	"Blank" configurations, signals are post-processed	Fixed set of sounding RIS profiles	Fixed set of sounding RIS profiles
Who collects measurements	BS	RIS	BS	BS

Synchronisation	unsynchronized	unsynchronized	unsynchronized	unsynchronized
Metric optimised	MSE for RF mapping; RMSE for localisation	Localisation accuracy	MSE for RF mapping; RMSE for localisation	SNR and CRB

#D-1: Graph-based radio map cartography for RIS-aided fingerprinting localisation

Please refer to D5.2 [RISED52] for an extended description of this contribution.

#D-2: OnRMap: An Online Radio Mapping approach for large intelligent surfaces

Motivation and context

Emerging technologies in beyond fifth generation of telecommunications demand sensing and localisation capabilities along with communications systems. One of the candidates' topologies for indoor systems is the Large Intelligent Surfaces (LISs), a large antenna array capable of transmitting and receiving electromagnetic signals and covering large areas. Such a characteristic is an enabler for high-resolution radio mapping (RMap), *i.e.,* translating electromagnetic signals into an environment representation through radio maps (RMs). We illustrate an indoor environment with a LIS covering the whole ceiling of a room in Figure 3-27.
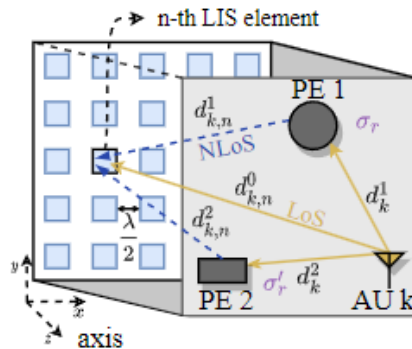

Figure 3-27. System model [HLS+23]

Methodology

The objective is to detect and localize standing humans, namely passive users, in a scenario containing metallic objects by performing RMap using K active users (AUs) training signals, *i.e.,* orthogonal pilots. To map the environment, we rely on the NLoS signals, which represent the bouncing in the R passive elements (PEs), while the LoS gives us the AUs localisation straightforward in RMap. The framework is composed of i) estimation of LoS and NLoS through a matched filter (MF) and robust component analysis (RPCA), ii) separation of the NLoS by translating the output data of RPCA using k-means and boundaries estimation algorithm, and iii) inference by density-based spatial clustering of applications with noise (DBSCAN) and correlating the energy contained in NLoS estimation. We refer to the whole process as OnRMap.

The interested reader can refer to [HLS+23] for all the details on the system model, problem formulation, and algorithmic solutions.

Results and outcomes

Figure 3-28 presents a single realization visual output of the OnRMap steps. The algorithm accuracy and detection rate were evaluated through a thousand Monte Carlo iterations and compared to [CVR+23] method. The detection rate and accuracy are shown in Figure 3-29. Compared to the reference, we highlight that OnRMap does not rely on a training phase. Thus, this method suits dynamic environments and needs minimal *a priori* knowledge of the environment. The main trade-off is in the detection rate *versus* localisation accuracy, where the proposed method misses more detections while having higher accuracy than the reference. At last,

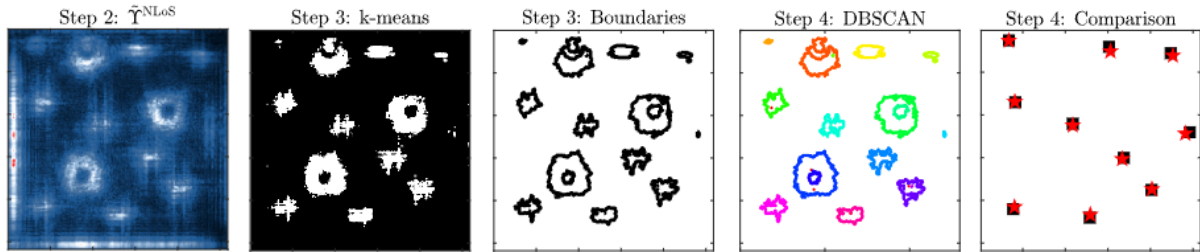Figure 3-30 shows the complementary cumulative distribution function in detection rate *versus* number of AUs.
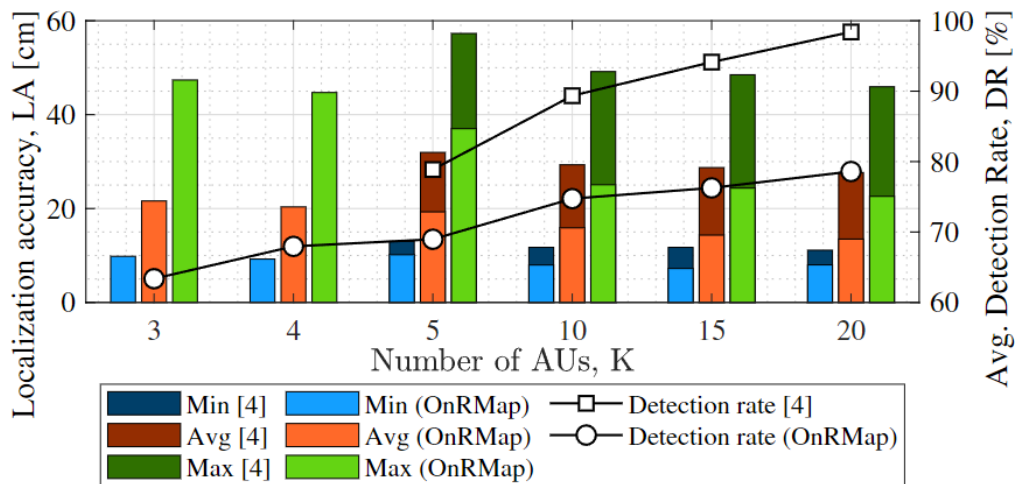

Figure 3-28. Example of application of OnRMap [HLS+23]

Figure 3-29. Average localisation accuracy and average detection rate for different number of AUs [HLS+23]. [4] refers to [CVR+23].
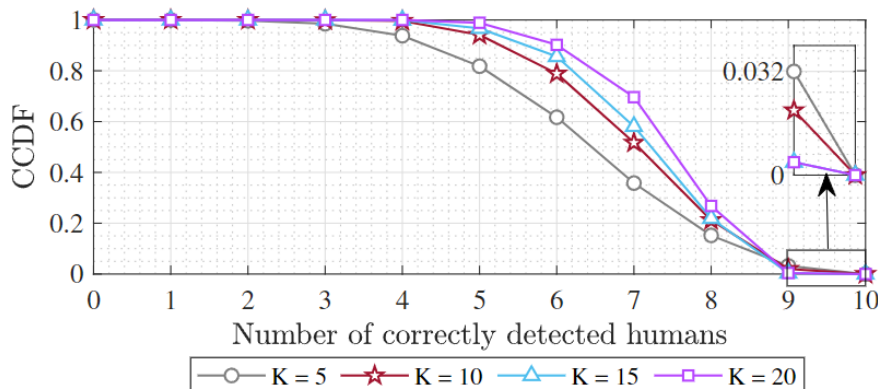
Figure 3-30. CCDF of the number of correctly detected humans for different numbers of AUs [HLS+23] .

Perspective and relation to other WP5 contributions

Sensing and localisation are key enabler for 6G technologies. The proposed framework provides an online and robust to dynamic environments method to detect humans using a LIS. The position of the passive users retrieved by this contribution can be used as side-information to increase the estimation accuracy of other WP5 contributions, by, for example, removing the effects of the passive users in an active users localisation algorithm.

#D-3: RIS-Aided Wireless Fingerprinting Localisation based on Multilayer Graph Representation

Motivation and context

Recently, WFL empowered by RISs has emerged as a powerful technique for enhancing the accuracy of mobile user localisation. WFL exploits the flexibility of RISs to generate a set of signal fingerprints, which are compared to the ones contained into pre-stored radio maps for localisation purposes. This avoids the need of having a large set of known anchors, such as base stations or access points, to create enough fingerprints for user localisation and thus reducing the overall cost of the system. However, many approaches proposed in literature, e.g., [NGG20] [ZWD+22], require access to the full radio maps, which is typically a costly and time-consuming process, as it needs to perform many measurements at different locations. To cope with the possible lack of Received Signal Strength Information (RSSI) at certain locations, in the deliverable D5.2 [RISED52], has been introduced a method for RF map cartography which interpolates several RF maps (one for each fingerprint) from a subset of collected measurements exploiting *graph* signal processing tools.

In this deliverable, to improve localisation accuracy, a novel method for WFL empowered by RISs is proposed, where the RSSI measurements are modelled as signals defined over a *multilayer graph*, which encodes data similarities across *both* the spatial and the fingerprints domains [SDB23]. Differently from graph-based approach [R17], the RISs are explicitly considered either in the construction and in the interpolation of the radio maps. Exploiting model-generated fingerprints, we can learn the multilayer graph topology that enables the use of graph-based sampling methods to recover the full radio map from the observation of subsets of measurements.

Methodology

The fingerprinting-based strategy proposed in this work aims to retrieve radio maps from RSSI measurements and then use these maps for mobile user localisation. Exploiting the intra- and inter-layers connectivity grasped by the multi-layer graph, first is found a bandlimited representation of the graph signal enabling the use of graph sampling theory. Then, the radio maps are recovered from the observation of a restrict number of measurements (samples). Specifically, the proposed learning and localisation strategy consists of the following three-steps:

1) *Learning Multilayer Graph and Signal Representation.* Assuming the radio map signal model as in [WD20], [GAT+22], a set of training RSSI vectors is generated. These vectors are used to learn the structure of the multilayer graph, which incorporates the correlation of these model-generated signals, jointly in the spatial and fingerprints domains. Then, sparse graph signals representations are derived by solving a basis pursuit problem which keeps the representation error below a required accuracy threshold.

2) *Sampling and Recovering of the RSSI Radio Maps.* Given the learned multilayer graph, Max-Det greedy sampling strategy in [TDB16] is applied to select a subset of nodes from which to gather observed field measurements. Then, exploiting the signal bandlimitedness enforced by the sparse representation, the network operator may recover the full maps from the RSSI sampled measurements by using graph sampling theory [TDB16]. It has been shown, through extensive numerical results, the robustness of the proposed strategy, assuming that the fingerprints correlations between the layers of the multilayer graph are not significantly varying with respect to the model-generated maps. The developed method enables to recover the radio maps from a reduced number of sensors by providing the positions where these sensors should be placed. This implies that only a reduced number of measurements instead of the overall maps need to be collected by the network operator in order to recover the full maps.

3) *Mobile user localisation.* The recovered maps can be then used for WFL applications. Specifically, the set of field measurements collected by the UE at some unknown positions are compared with the recovered maps. To estimate the UE position several criteria can be adopted, as for example a minimum distance (MD) or a maximum correlation

coefficient (MCC) criterion [NGG+21]. To improve localisation accuracy, it is also applied a k-nearest neighbour (kNN) method by computing the estimated UE location as the average of the locations corresponding to the first k best coefficients of the MD or MC criteria.

Results and outcomes

To assess the effectiveness of the proposed methods, the 2D propagation scenario is considered, as illustrated in Figure 3-31, composed of a single BS (red square) and two RISs (green squares), each modelled as a uniform linear array with M=25 elements spaced by λ/2. The BS emits signals at frequency of 1GHz with a transmission power equal to 5dB. The multilayer graph is composed of P=4 layers and we associate with each layer the RSSI fingerprint generated by a given RIS configuration. The field is observed over an area of 10x20 m^2 at locations corresponding to the N=150 nodes of a grid graph, placed at a distance of 1m.

First, the multiplayer graph can be learned from the model-generated signals, and then a sparse radio map representation can be found using as bases the eigenvectors of the inferred multilayer graph. To assess the trade-off between sparsity (compression) and accuracy, in Figure 3-32 it is reported the average sparsity of the signals versus the radio map normalized mean squared error (NMSE), assuming, for this experiment, the observed signal to be noiseless. The proposed multi-layer approach is compared with a graph-based recovering method that considers as signal basis the eigenvectors of the Laplacian matrix associated to a single layer. It can be observed as multi-layer graphs provide a remarkable better trade-off between sparsity and signal estimation accuracy than graph-based method. This gain is due to the capability of the multi-layer topology to encode the interactions among multiple RSSI fingerprints.

Furthermore, to better investigate the impact of the estimation error value on the RSSI map recovering, in Figure 3-31 is reported an example of the true original field (left plot) and recovered map (right plot) obtained using an average number of samples for layer equal to 60 and with a signal NMSE=0.19. It can be noticed the goodness of the recovered field by using only the 40% of the overall layer measurements.

To evaluate the effectiveness of the proposed RIS-aided fingerprint localisation, the MD and MCC localisation strategies are applied by using the recovered radio maps. The mobile users are randomly placed within the area of interest, and they observe a noisy RSSI field affected by Gaussian noise with zero-mean and standard deviation σ. Then, in Figure 3-33 is shown the localisation mean error, averaged over 100 random user positions and over 100 noise random realizations, versus σ and for different values of the number P of RIS configurations used in the localisation phase. The kNN-based localisation strategies are applied with k=4 neighbours by comparing the two localisation strategies MD and MCC for the scenario in Figure 3-31. It can be noticed as, in the observed scenario, the MD strategy reaches better performance than the MCC method, by keeping close to the case where the true maps are used for UEs localisation.

As further numerical example, Figure 3-34 illustrates the localisation mean error versus the number of RIS configurations for different noise variance. It can be observed the high robustness of the method to the noise degradation.

Finally, in Figure 3-35 our proposed multi-layer graph method is compared with the graph-based learning strategy proposed in [R17], and with a kernel-based signal interpolation that exploits a standard Gaussian kernel. The mean localisation error versus the number of the RIS configurations is reported in the noiseless case and by applying the MD criterion. For all methods, is used a number of average samples over each graph (layer) equal to 20. It can be noticed that the proposed multi-layer-based localisation method exhibits considerable performance gain compared with both the graph-based method in [R17] and the kernel-based interpolation approach. This accuracy enhancement is due to the capability of the proposed strategy to exploit the fingerprint domain, thus keeping its performance very close to the ideal case where the true maps are employed for localisation.
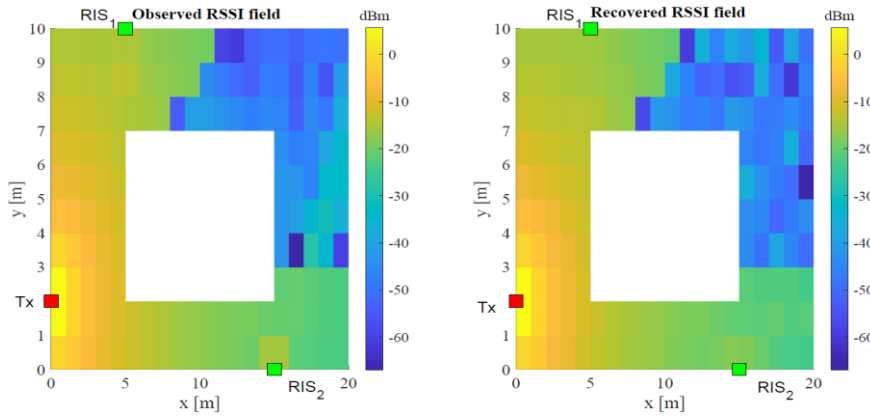
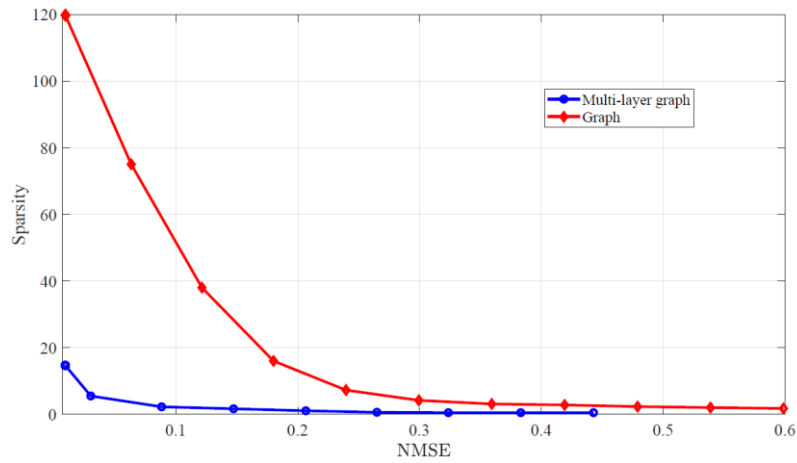**Figure 3-31. Observed (left) and learned (right) RSSI field.**

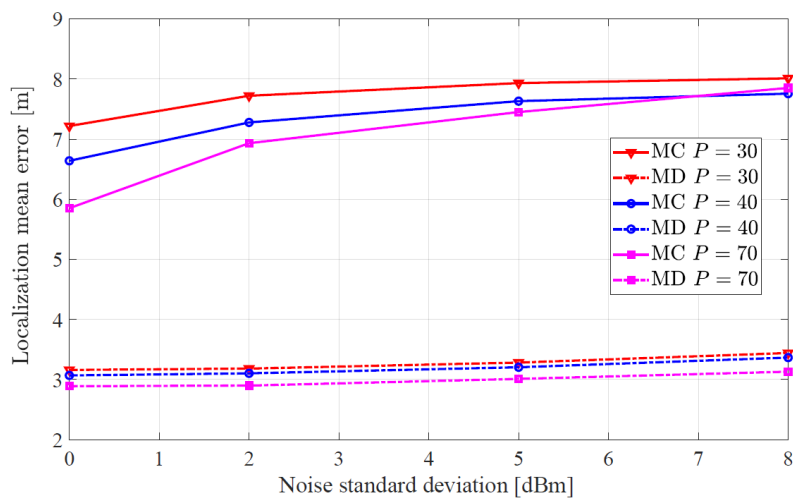**Figure 3-32. Trade-off sparsity vs NMSE.**

Figure 3-33. Localisation mean error vs σ for different number of RIS configurations.
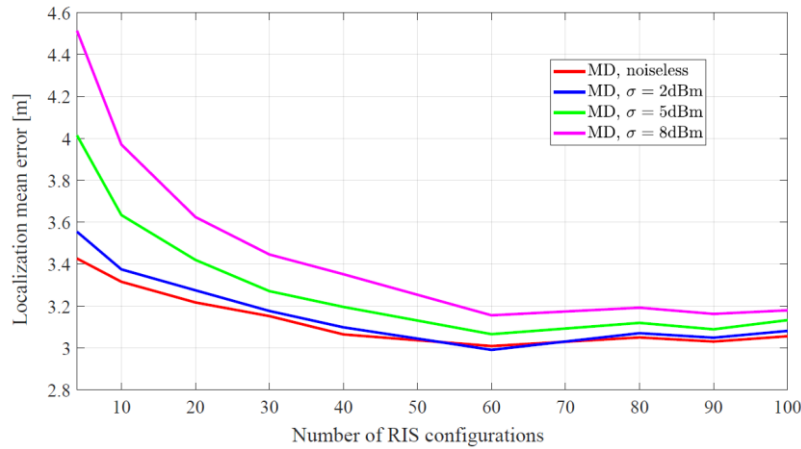
Figure 3-34. Localisation mean error vs the number of RIS configurations,

for different noise variance.
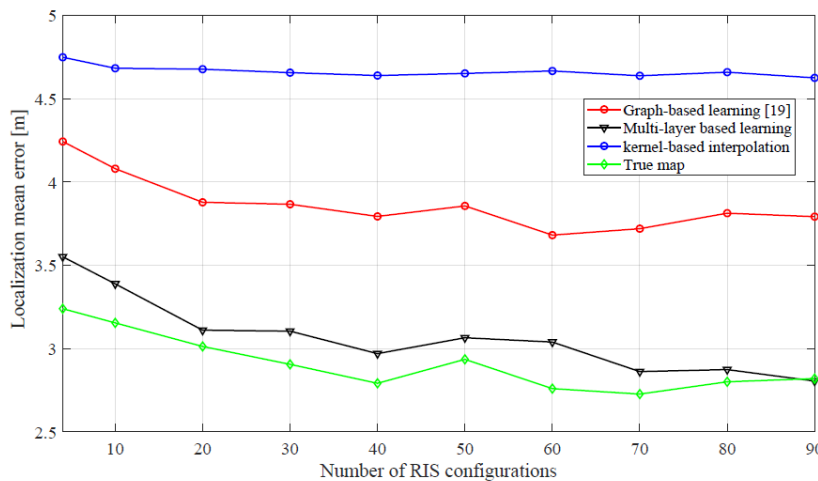
Figure 3-35. Localisation error vs. the number of RIS configurations.

Perspective and relation to other WP5 contribution
Since this work proposes a general method for EM radio map interpolation, it can be used also in other WPs for spatial information-based resource allocation to, e.g., reduce EMF absorption within specific regions while maximizing communication performance in other areas.

#D4: Practical AI-assisted RIS planning

Motivation and context
In our work, we propose D-RISA, namely Deep RIS-Aware network deployment and planning, as a novel deep reinforcement learning (DRL)-based solution to enable practical installation of RISs in the field, using a raytracing simulation of the target area.

We introduce a paradigm shift in the use of DRL to solve RIS deployment problems by not aiming at producing a DRL agent able to solve any problem instance, but rather tailoring the training of D-RISA to the specific problem at hand, making it less demanding w.r.t. the available

---

literature while avoiding the discretization of the solution space and thus increasing the solution scalability.

In particular, the contributions can be summarized as follows: we i) translate the RIS deployment problem into a DRL problem by means of the bespoke space and action spaces design, ii) identify the minimum SNR that directly translates into maximum localisation accuracy as a feasible metric to be computed by a custom-made ray tracing simulator to feed the DRL training process, iii) make use of the D-RISA DRL agent training phase as an exploration tool to find the best deployment solution, avoiding the need for a complete viable agent, iv) showcase the rapid convergence of the agent solution and v) benchmark D-RISA against the State-of-the-Art (SOA) as well as exhaustive approaches, demonstrating outstanding performance while emulating the indoor scenario of a real environment, namely Rennes Railway Station in France.

Methodology

We tackle the problem of efficiently deploying RISs in a known environment. We extend a currently existing network deployment with RISs to eliminate coverage dead zones. We consider the environment of the Rennes railway station hall, operated by the French Société Nationale des Chemins de fer Français (SNCF), and visualized in Figure 3-36. We try to alleviate in particular the dead zone problem. The current deployment of BSs in the Rennes station has several areas with connectivity problems due to the low SNR achieved. We identify and set Test Points (TPs) on those locations and alleviate the problem with our proposed solution. Specifically, we make use of a custom-made ray tracing engine to simulate any proposed deployment in the scenario while accounting for its current network infrastructure, provided by a major European network operator. As the ray tracer outputs the values of the objective function (the minimum SNR across all the TPs defined, as described in Section III) we train a DRL solution by using them as rewards.
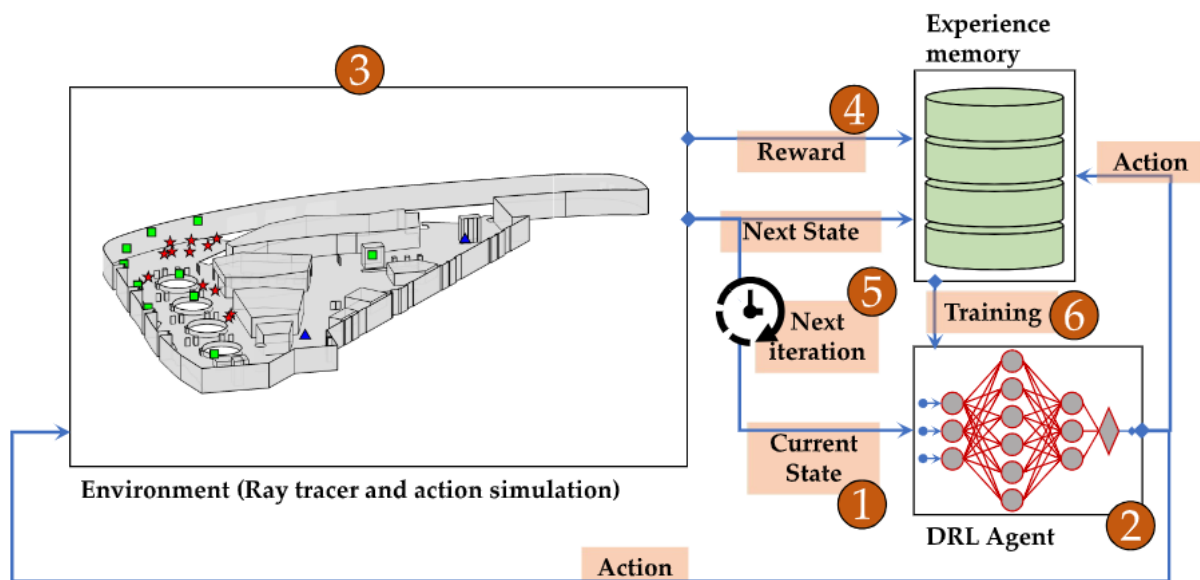
Figure 3-36. D-RISA's building blocks showing the training process for a given frame. In the 3D map, the candidate sites (CSs) for the RIS deployment are shown in green, the BSs in blue, and test points (TPs) in red.

We showcase the main building blocks of our proposed solution, itemizing the operations required for a single training cycle iteration. Here we only assess the main components of D-RISA, namely i) a 3D model of the scenario, ii) a ray tracer running on such scenario and capable of evaluating candidate deployment solutions, iii) a model for the RIS gain, which we use in combination of the ray tracer to numerically evaluate any solution, iv) a Deep Q-Learning (DQL)

agent, which takes as input a given solution and decides the best among the different potential changes on it, purposely with the long-term goal of improving our objective, and v) the training process of said agent, following the principles of Deep Q-learning from Demonstrations (DQfD). We would like to underline that DQL is only one flavour of DRL and that D-RISA can be readily extended to other DRL techniques with minimal modifications.

Results and outcomes

We consider the Rennes railway station scenario. D-RISA does not impose a restriction on the existing infrastructure, and increasing the number of pre- deployed BSs has a negligible impact on the computational costs. Nevertheless, for this work, we reproduce in the ray tracer the currently existing installation of radio equipment in the location by the operator. Thanks to this parallelism, we are able to assess that current coverage problems are reproduced in our simulations, confirming their predictive capability, and we can obtain practically useful and applicable solutions. This infrastructure is characterized by $M = 2$ existing BSs with a transmit power $P = 28$ dBm operating at $f = 26$ GHz, and select $N = 10$ CSs, and $T = 13$ TPs. The coverage of the area, the positions of the existing BSs and their properties are provided by the European major network operator serving the station. The TPs are scattered in the area, focusing on the sectors wherein existing BSs are not able to provide adequate coverage, while the CSs are handpicked in architecturally suitable places, both in areas directly surrounding the TPs and outside the immediate vicinity, as depicted. The ray tracer uses a 3D model of the station, which reproduces the most prominent architectural features of the environment. The model is composed of a total of 579 triangular surfaces. It uses the SBR method to find all possible paths between any pair of given points. For simplicity, we use a single material for the whole environment as a reference to compute the losses at each reflection. The material properties are in agreement with the International Telecommunication Union (ITU) values for the permittivity and conductivity of concrete at $f = 26$ GHz, i.e., real part of relative permittivity $Re(\varepsilon_r) = 5.31$, and conductivity $\sigma = 0.4557$ S/m. To compute the overall effect of the deployment of RISs in our scenario beyond the chosen test points, we also analyse the whole surface at a height of 1.5m.
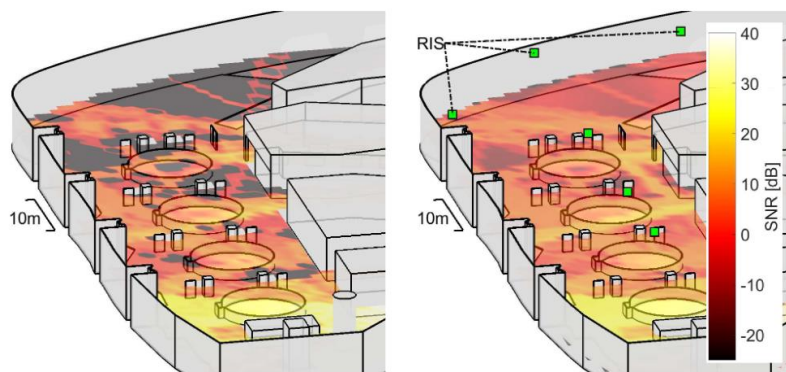
Figure 3-37. SNR analysis considering the current arrangement (left) and the SNR achievable with L = 6 RISs (right).

To produce such heatmaps, we model the RISs as isotropic scatterers. We can see the difference between the current deployment without RISs in Figure 3-37. We employ a multi-layered perceptron (MLP) neural network (NN) design with 2 hidden, fully connected layers of 32 neurons activated via a rectified linear unit (ReLU) function. The learning rate and the future reward reduction are respectively set to $\eta = 0.00025$ and $\gamma_q = 0.99$, which are optimized by means of the Adam algorithm. The training period of the primary network NN is $TT = 4$ complete frames and the period between updates of the secondary network NN' (i.e., by copying NN) is $TST = 500$ complete frames. We apply our solution to the described scenario, and put it side-by-side with the following benchmarks: i) the solution obtained by exhaustive search (ES), ii) the solution

obtained by ES considering clusters of TPs instead of individual TPs, drastically reducing the number of possible associations and allowing us to extend the ES up to L = 4, iii) the solution obtained by means of the State-of-the-Art RISA, which is based on FP, and iv) a statistical average of random solutions as previously obtained in the same scenario. D-RISA outperforms all other solutions and matches the ES approaches in terms of minimum SNR (i.e., maximum localisation accuracy) at a much lower computational cost.
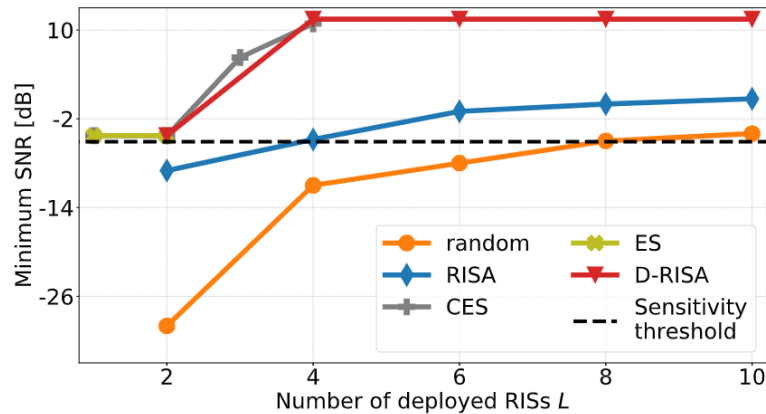

Figure 3-38. D-RISA performance against benchmark methods and State-of-the-Art RISA for a different number of deployed RISs in terms of minimum SNR.

D-RISA training. We observe an increasing trend in solution performance as the agent keeps building its ability to improve deployments. As the training process ends with an exploitative behaviour, the high values of the best normalized minimum SNR during each episode suggest that the agent has learned a successful strategy to solve the problem even without exploratory actions. In some instances, the agent might be unsuccessful in solving the problem at the training end just by leveraging on its own knowledge (exploitation). Nonetheless, the overall training process is still able to produce a good solution for the RIS deployment problem by combining the exploration and exploitation strategies. If the training time is extended past solution convergence, the relative improvements on the best normalized SNR decrease: the fully trained agent does not further improve its output by adding more training effort. This hints at the fact that the most value of D-RISA is obtained early in the training, thus allowing for shorter training times and reducing the computational complexity.

Perspective and relation to other WP5 contribution
This contribution proposes an AI-based method for RIS planning pursuing optimized sensing and localisation. It can be used as a model interplaying with WP3 contributions as well as with control mechanisms proposed in D5.3 [RISED53].

4 Practical algorithms for laboratory demonstrations and field trials of RIS-aided localisation, mapping, and sensing

In this section, we detail some concrete experimental setups with corresponding scenarios that will be considered in WP7 for both the laboratory demonstrations and the field trial experiments of WP5 localisation and sensing algorithms. As for the final results of these experimental validations, they will be accounted in the final D7.3 deliverable.

The mapping of the lab demos and field trials to the contributions from Section 3 is provided in Table 4-1.

Table 4-1 Relation between demos and trial to the contributions.

Demo/ trial	Related contributions	Comments
Demo at 3.7 GHz: RIS-aided finger-printing positioning	Cont. #D-3: RIS-Aided Wireless Fingerprinting Localisation based on Multilayer Graph Representations	The proposed WFL algorithm is based on radio maps, built on lab measurements, and corresponds to the final part of Cont. #D-3, where collected fingerprints are replaced with a radio map recovered applying multilayer graph topology methods.
Demo at 27 GHz: mmWave RIS with SAGE algorithm	Cont. #A-1: Far-field ToA and AOD estimation of a signal reflected by a RIS Cont. #B-2: RIS-Enabled SISO Localistion under User Mobility and Spatial-Wideband Effects Cont. #C-5: RIS-enabled sensing with single- and double bounce-signals	Cont. #C-5 is applied to generate multiple hypotheses of the UE location.
Demo at 60 GHz: RIS-Aided Self-UE Localisation	Cont. #A-1: Far-field ToA and AOD estimation of a signal reflected by a RIS Cont. #B-3: RIS-Enabled Self-Localisation: Leveraging Controllable Reflections with Zero Access Points Cont. #C-1: RIS-Enabled Self-localisation and SLAM with Zero Access Points	
Online field trials	Cont. #A-1: Far-field ToA and AOD estimation of a signal reflected by a RIS Cont. #B-2: RIS-Enabled SISO Localisation under User Mobility and Spatial-Wideband Effects Cont. #D-3: RIS-Aided Wireless Fingerprinting Localisation based on Multilayer Graph Representations	Cont. #D-3 is a back-up solution.

4.1 Lab-demos

4.1.1 Demo at 3.7 GHz: RIS-aided fingerprinting positioning

The purpose of this demonstration is to show the feasibility of localizing a UE with the aid of a RIS and a BS, even in a cluttered environment at low carrier frequencies.

Measurements will be collected in an indoor office environment. We consider that the BS (Tx) and the RIS are in two different fixed locations, while the UE (Rx) can assume L different positions inside a specific area A.

The RIS-aided wireless fingerprinting localisation process is performed in two phases:

- We collect the RSSI values received by the UE to form two fingerprint databases of the position grids. The first database (*DB-DL*) is established in a scenario without the RIS, where the transmitter (BS) and the receiver (UE) communicate through a direct link. We collect a vector of L fingerprints $\tilde{r} = [\tilde{r}_1, \ldots, \tilde{r}_L]$, corresponding to each position $l \in [1, \ldots, L]$ assumed by the UE in the location grid. The second database (*DB-RIS*) is compiled in a scenario where no direct link can be established between the BS and the UE (blockage event), and we leverage a RIS-aided communication link. The BS transmits continuous pilot signals, while the RIS cycles through M different configurations. Then, for each position l assumed by the UE, we collect the RSSI values exploring each $m \in [1, \ldots, M]$ RIS configuration, forming a fingerprints matrix $\hat{R} = [\hat{r}_1, \ldots, \hat{r}_M]^T \in R^{M \times L}$.

- During the second phase, the UE is placed at an unknown position $x \in A$. Thus, we collect from the BS a single RSSI value received $\tilde{s}_x$, in case of *DB-DL*, or a vector of M signal strength measurements $\hat{s}_x = [\hat{s}_1, \ldots, \hat{s}_M]^T$, in case of *DB-RIS*. The localisation is performed by comparing the current RSSI received in x with the values stored in the databases. To estimate the UE position, several criteria can be adopted, as for example a minimum distance (MD) or a maximum correlation coefficient (MC) criterion [NGU21]. In particular, we can find the most likely location l^* as follows. Denoting by $\widetilde{R}(l)$ the l-th column of the matrix $\widetilde{R}$, the MD method returns the optimal position l^* of the UE, in case of database *DB-RIS*, such that it holds the following

$$l^* = \arg\min_{l \in [1,L]} \ d_p(l) \coloneqq \left\| \widetilde{R}(l) - \hat{s}_x \right\|_F$$

while the MC criterion takes a decision for the UE position l^* according to the following rule

$$l^* = \arg\max_{l \in [1,L]} \ \rho(l) \coloneqq \frac{\widetilde{R}(l)^T \hat{s}_x}{\left\| \widetilde{R}(l) \right\|_F \|\hat{s}_x\|_F}.$$

The same criteria can be applied in case of database *DB-DL* by comparing $\tilde{r}$ and $\tilde{s}_x$. To improve localisation accuracy, we can apply a kNN method hinging on the MD and MC strategies. Specifically, we sort the coefficients $d_p(l)$ and $\rho(l)$ in increasing and decreasing order, respectively, and for each strategy we compute the estimated UE location as the average of the locations corresponding to the first k coefficients.

The performance in the location estimate is measured through the RMSE, with the intention to show that fingerprinting localisation based on *DB-RIS* is better than the one based on *DB-DL*.

4.1.2 Demo at 27 GHz: mmWave RIS with SAGE algorithm

The experimental setup for this measurement campaign relies on a VNA-based mmWave channel sounder and includes a Transmit-RIS (TRIS) on the transmitter side and a Reflective-RIS (RRIS) positioned between the transmitter and the receiver (RX), both equipped with 1-bit element-wise phase control. Referring to the RRIS as "RIS" and the TRIS as "BS" for simplicity, the measurement acquisition involves azimuthal beam scanning by the BS from -60° to +60° in 5° increments while the RRIS remains inactive. Following this, the BS illuminates the activated RRIS with a static beam, which then undergoes beam sweeping with the same orientation configurations. We harness the high-resolution Space-Alternating Generalized Expectation-maximization (SAGE) algorithm which allows us to discern crucial properties of Multipath Components (MPCs), such as their delays, Angles of Arrival (AoAs), and associated gains. The MPCs extracted pertain to both the direct path between the BS and UE, and the reflected path via the RIS before reaching the UE. Prior to the application of SAGE, meticulous characterization and calibration of the impact of cables and RF components within the acquisition chain are carried

Document: H2020-ICT-52/RISE-6G/D5.4
Date: 29/09/2023   **Security:** Public
Status: Final   **Version:** 1.0

out. Once parameters are extracted, the focus shifts to localisation. Specifically, AoD estimates are deduced through a combined process of beam sweeping at both the BS and the RIS and the extraction of MPCs.

4.1.3 Demo at 60 GHz: RIS-Aided Self-UE Localisation

This setup involves a UE (a radar transceiver) and a RIS. The objective is to localise the UE with aid of the RIS, using backscattered signals from the RIS.

Channel Parameter Estimation: The UE transmits the chirp signals. When the UE receives the back-propagated signals including the loop-back propagation from the RIS, the beat signals at an intermediate frequency are observable. The observed signals are analysed with the different frames, where 1 frame consists of 128 chirps (slow-time domain), and 1 frame consists of 600 samples (fast-time domain). By the 2D FFT of each frame, we generate the range-Doppler map and determine the range and Doppler pairs to the targets, including the RIS. Over 4 RX antennas, 4 complex values corresponding to the estimated range and Doppler can be selected, and 1D FFT is adopted to estimate the AoD of targets.

UE Localisation with Data Association: In the range domain, the three largest peaks could be detected. The first is the self-interference at the UE, the second is the physical reflection from the RIS, and the last is the loop-back signal from the RIS. Using the second and third peaks with the known RIS location, we determine the parameters associated with the RIS. Then, the UE location is estimated by the geometric relations or 2D search with the ML estimator.

4.2 Online field trials

The field-trial demonstration will be performed in a real scenario to validate how a 3D UE localisation process can be realized. In particular, the field-trial demonstration will take place in CRF premises (Turin) to showcase specific kitting operations where positioning is of paramount importance for AGV operations. Final details will be provided in the deliverable D7.3. The testing scenario will include 2 mmWave RISs that will be exploited to infer the target position via RSRP measurements.

Hardware equipment and main system specifications

The current system set-up is composed of:
- *BS*: a commercial Ericsson 5G NSA BS, equipped with the RF module AIR5322 operating at N258 band (licensed TIM frequency band is 26.9-27.1 GHz). The 5G BS antenna array can be configured to force the transmission of a specific broadcast beam among 24 ones available: azimuth angle ranges between -60 and +60° is split into 3 different beams, while elevation angle ranges between -15 and +15° and it is spit into 8 different beams;
- *5G-Core:* TIM 5G *commercial* core network to realize a full end-to-end 5G connection with the UE equipped with a live network SIM;
- *UE terminal*: a 5G CPE by ZTE, which allows to read SS-RSRP values in real-time while being connected to the BS/5G network;
- *R-RIS*: the RIS is the same as the one already used for in-lab offline demonstration, whose element phase distribution is optimized at 27 GHz. The RIS can be configured to steer the reflected beam toward specific directions.

In addition, a VIAVI signal analyser is provided to support setting up operations.

Operational scenario

The localisation principle can be summarized as follows (see Figure 4-1):

- A BS transmits signals sequentially towards each R-RIS, The BS has location $\mathbf{x}_{BS}$, RIS-A has location $\mathbf{x}_A$ and orientation $\mathbf{R}_A$ (similarly for RIS-B). The user has location $\mathbf{x}_{UE}$.
- Both RISs can be dynamically configured to change the reflected signal direction (directional beams) and sweep over a large area where the user might be located.
- During the time the BS transmits signals towards RIS-A, RIS-A applies directional beams (say $\mathbf{f}_1,…,\mathbf{f}_N$) towards a set of possible UE locations (say $\mathbf{x}_1, …, \mathbf{x}_N$), according to a deterministic pattern enabling to scan the environment in azimuth.
- For each beam, the UE measures the received power (say, $p_1, …, p_N$ for RIS-A and $q_1, …, q_N$ for RIS-B). Note that the locations are defined in a global frame of reference, so that a beam towards location $\mathbf{x}_i$ in a global frame of reference is considered to be towards $\mathbf{R}_A^T (\mathbf{x}_i - \mathbf{x}_A)$, in the local frame of reference of the RIS-A (similarly for RIS-B). Also note that the transmit power of the BS is set to be minimum.
- For each candidate point in the set of possible UE locations, a controller connected to both RISs and UE computes a weight $w_i = (p_i + q_i)/(\Sigma_j\ p_j + q_j)$, based on received powers. Then, the pairs (w_i, $\mathbf{x}_i$) represent a probability mass function of the UE location, which somehow accounts for the probability that the UE lies in each candidate test/trial location.
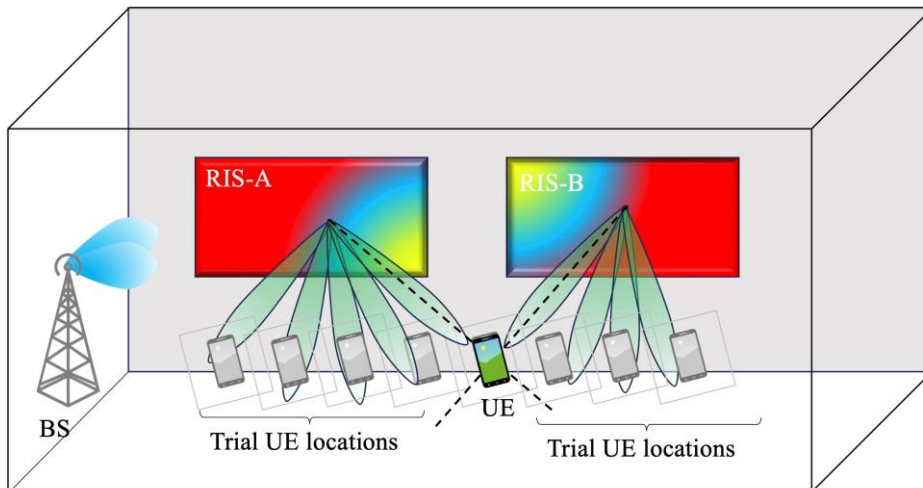

Figure 4-1: Principle of the online field trial for single-BS RIS-aided single-BS localisation within commercial network (the so-called "trial" locations correspond to the tested candidate UE locations) [KDA+22].

5 Conclusions

Reconfigurable Intelligent Surfaces (RISs) possess significant potential for exerting control over radio wave propagation and manipulating the geometry of multipath-aided localisation issues. This capability potentially empowers the realization of highly precise localisation and sensing, radio-frequency mapping, and the detection of obstacles and activities. This makes RISs particularly well-suited for scenarios where traditional architectural setups and deployments fall short. However, the integration of RISs represents a paradigm shift that necessitates the development of new techniques and algorithms.

This deliverable is to address this pressing need. It serves as a comprehensive guide, outlining innovative algorithms for channel estimation, localisation, and sensing designed to cater to a wide spectrum of scenarios. It plays a pivotal role in bridging the gap between WP5 and the expected RISE-6G project results, thereby acting as a final specification. These algorithms and techniques serve as building blocks for the advancement of RIS technology within the project, marking a significant step towards unlocking the full potential of RISs in next-generation wireless communication systems.

References

[3GPP10]	"Physical channels and modulation, release 16, V16.2.0," 3GPP, Sophia Antipolis, France, Rep. 3GPP TS 36.211, Mar. 2010.
[AVW22]	G. C. Alexandropoulos, I. Vinieratou and H. Wymeersch, "Localisation via Multiple Reconfigurable Intelligent Surfaces Equipped With Single Receive RF Chains," in *IEEE Wireless Communications Letters*, vol. 11, no. 5, pp. 1072-1076, May 2022.
[BAS97]	Brandstein, Michael S., John E. Adcock, and Harvey F. Silverman. "A closed-form location estimator for use with room environment microphone arrays." IEEE transactions on Speech and Audio Processing 5, no. 1 (1997): 45-50.
[BG06]	M. Biguesh, A.B. Gershman, "Training-based MIMO channel estimation: a study of estimator tradeoffs and optimal training signals," *IEEE Transactions on Signal Processing*, vol. 54, no. 3, pp. 884-893, 2006.
[BGV+22]	Balasubramanian, Anantharaman, Kapil Gulati, Dan Vassilovski, Shuanshuan Wu, Junyi Li, Sourjya Dutta, and Preeti Kumari. "Reconfigurable intelligent surface enabled sidelink position-ing." U.S. Patent 11,540,089, issued December 27, 2022.
[BSY19]	F. Bellili, F. Sohrabi, W. Yu, "Generalized approximate message passing for massive MIMO mmWave channel estimation with Laplacian prior," *IEEE Transactions on Communications*, vol. 67, no. 5, pp. 3205-3219, 2019.
[CKA+20]	G. K. Carvajal, M. F. Keskin, C. Aydogdu, O. Eriksson, H. Herbertsson, H. Hellsten, E. Nilsson, M. Rydström, K. Vänas, and H. Wymeersch. "Comparison of automotive FMCW and OFDM radar under interference," in 2020 IEEE Radar Conference (RadarConf20), 2020, pp. 1–6
[CKA+23]	Chen, Hui, Hyowon Kim, Mustafa Ammous, Gonzalo Seco-Granados, George C. Alexandrop-oulos, Shahrokh Valaee, and Henk Wymeersch. "RISs and sidelink communications in smart cities: The key to seamless localization and sensing." arXiv preprint arXiv:2301.03535 (2023).
[CVR+23]	C. J. Vaca-Rubio, P. Ramirez-Espinosa, K. Kansanen, Z. -H. Tan and E. d. Carvalho, "Radio Sensing with Large Intelligent Surface for 6G," ICASSP 2023 - 2023 IEEE International Conference on Acoustics, Speech and Signal Processing (ICASSP), Rhodes Island, Greece, 2023, pp. 1-5.
[CZK+23]	Chen, Hui, Pinjun Zheng, Musa Furkan Keskin, Tareq Al-Naffouri, and Henk Wymeersch. "Mul-ti-RIS-enabled 3D sidelink positioning." arXiv preprint arXiv:2302.12459 (2023).
[EAH18]	M. E. Eltayeb, T. Y. Al-Naffouri and R. W. Heath, "Compressive Sensing for Millimeter Wave Antenna Array Diagnosis," in IEEE Transactions on Communications, vol. 66, no. 6, pp. 2708-2721, June 2018, doi: 10.1109/TCOMM.2018.2790403.
[FKS+22]	Fascista, Alessio, Musa Furkan Keskin, Angelo Coluccia, Henk Wymeersch, and Gonzalo Seco-Granados. "RIS-aided joint localization and synchronization with a single-antenna receiv-er: Beamforming design and low-complexity estimation." IEEE Journal of Selected Topics in Signal Processing 16, no. 5 (2022): 1141-1156.
[GAT+22]	F. Ghaseminajm, M. Alsmadi, D. Tubail, and S. S. Ikki, "RIS-aided mobile localization error bounds under hardware impairments," IEEE Trans. Communic., vol. 70, no. 12, pp. 8331–8341, 2022.
[GCA+22]	R. Ghazalian, H. Chen, G. C. Alexandropoulos, G. Seco-Granados, H. Wymeersch, and R. Jäntti, "Joint user localization and location calibration of a hybrid reconfigurable intelligent sur-face," arXiv preprint arXiv:2210.10150, 2022.
[GGD+21]	A. Guerra, F. Guidi, D. Dardari, and P. M. Djuric, "3D Source Tracking with Large Antenna Arrays in the Fresnel Region," in Proc. IEEE International Workshop on Signal Processing Advances in Wireless Communications 2021 (IEEE SPAWC'21), pp. 426–430, 2021.

[GZJ+22]	Gu, Xiaohui, Guoan Zhang, Yancheng Ji, Wei Duan, Miaowen Wen, Zhiguo Ding, and Pin-Han Ho. "Intelligent surface aided D2D-V2X system for low-latency and high-reliability communications." IEEE Transactions on Vehicular Technology 71, no. 11 (2022): 11624-11636.
[HFA22]	He, Jiguang, Aymen Fakhreddine, and George C. Alexandropoulos. "Simultaneous indoor and outdoor 3D localization with STAR-RIS-assisted millimeter wave systems." In 2022 IEEE 96th Vehicular Technology Conference (VTC2022-Fall), pp. 1-6. IEEE, 2022.
[HFV+23]	J. He, A. Fakhreddine, C. Vanwynsberghe, H. Wymeersch, and G. C. Alexandropoulos, "3D localization with a single partially-connected receiving RIS: Positioning error analysis and algorithmic design," IEEE Transactions on Vehicular Technology, May 2023.
[HFW+23]	J. He, A. Fakhreddine, H. Wymeersch, and G. C. Alexandropoulos, "Compressed-sensing-based 3D localization with distributed passive reconfigurable intelligent surfaces," In IEEE International Conference on Acoustics, Speech, and Signal Processing, Rhodes, Greece, pp. 1–5, June 2023.
[HLS+23]	Santos, H. L., Croisfelt, V., J., C., Abrao, T., & Popovski, P.. OnRMap: An Online Radio Mapping Approach for Large Intelligent Surfaces. 2023, ArXiv preprint arXiv:2302.02638
[HRD08]	Haardt, Martin, Florian Roemer, and Giovanni Del Galdo. "Higher-order SVD-based subspace estimation to improve the parameter estimation accuracy in multidimensional harmonic retrieval problems." IEEE Transactions on Signal Processing 56, no. 7 (2008): 3198-3213.
[KDA+22]	K. Keykhosravi, B.Denis, G.C. Alexandropoulos, A. Albanese, V. Sciancalepore, S. He, H. Wymeersch, "Leveraging RIS-Enabled Smart Signal Propagation for Solving Infeasible Localisation Problems", arXiv preprint arXiv:2204.11538, Avril 2022.
[KCK+22]	Kim, Hyowon, Hui Chen, Musa Furkan Keskin, Yu Ge, Kamran Keykhosravi, George C. Ale-xandropoulos, Sunwoo Kim, and Henk Wymeersch. "RIS-enabled and access-point-free simul-taneous radio localization and mapping." arXiv preprint arXiv:2212.07141 (2022).
[KFC+22]	Kim, Hyowon, et al. "RIS-Aided Radar Sensing and Object Detection with Single and Double Bounce Multipath." arXiv preprint arXiv:2212.07142 (2022).
[KKS+22]	Keykhosravi, Kamran, Musa Furkan Keskin, Gonzalo Seco-Granados, Petar Popovski, and Henk Wymeersch. "RIS-enabled SISO localization under user mobility and spatial-wideband effects." IEEE Journal of Selected Topics in Signal Processing 16, no. 5 (2022): 1125-1140.
[KSA+22]	K. Keykhosravi, G. Seco-Granados, G. C. Alexandropoulos, and H. Wymeersch, "RIS-Enabled Self-Localisation: Leveraging Controllable Reflections with Zero Access Points," in *Proceedings of IEEE International Conference on Communications*, Seoul, South Korea, 16–20 May 2022.
[LCT+22]	Y. Lu, H. Chen, J. Talvitie, H. Wymeersch, and M. Valkama, "Joint RIS calibration and multi-user positioning," in 2022 IEEE 96th Vehicular Technology Conference (VTC2022-Fall). IEEE, 2022, pp. 1–6.
[LLH+16]	J.-J. Lin, Y.-P. Li, W.-C. Hsu, and T.-S. Lee, "Design of an FMCW radar baseband signal processing system for automotive application," SpringerPlus, vol. 5, 12 2016.
[NGG20]	C. L. Nguyen, O. Georgiou and G. Gradoni, "Reconfigurable intelligent surfaces and machine learning for wireless fingerprinting localization," arXiv preprint arXiv:2010.03251, 2020.
[NGG+21]	Nguyen, C. L., Georgiou, O., Gradoni, G., & Di Renzo, M. (2021). Wireless Fingerprinting Localisation in Smart Environments Using Reconfigurable Intelligent Surfaces. *IEEE Access, 9,* 135526-135541.
[PRL+18]	J. A. del Peral-Rosado, R. Raulefs, J. A. LÃspez-Salcedo, and G. Seco-Granados, "Survey of cellular mobile radio localisation methods: From 1G to 5G," IEEE Commun. Surveys Tuts., vol. 20, no. 2, pp. 1124– 1148, 2018.
[R17]	A. E. C. Redondi, "Radio map interpolation using graph signal processing," IEEE Communic. Letters, vol. 22, no. 1, pp. 153–156, 2017.

[RDK+21]	M. Rahal, B. Denis, K. Keykhosravi, B. Uguen, H. Wymeersch, "RIS-Enabled Localisation Continuity Under Near-Field Conditions", Proc. IEEE SPAWC'21, Sept. 2021. Pre-print available on ArXiv: https://arxiv.org/abs/2109.11965
[RHD14]	F. Roemer, M. Haardt, & G. Del Galdo, "Analytical performance assessment of multi-dimensional matrix-and tensor-based ESPRIT-type algorithms," *IEEE Transactions on Signal Processing*, vol. 62, no. 10, pp. 2611-2625, 2014.
[RISED23]	M. Crozzoli, et al. "Reference System, Scenarios and Use Cases Analysis: Final Results", Deliverable D2.3 of the RISE-6G Project, Feb. 2022
[RISED24]	V. Sciancalepore et al., ''Metrics and KPIs for RISE Wireless Systems Analysis: First Results", Deliverable D2.4 of the RISE-6G Project, Feb. 2022
[RISED51]	H. Wymeersch et al., ''Control for RIS-based Localisation and Sensing (Intermediary Specifications)", Deliverable D5.1 of the RISE-6G Project, April 2022
[RISED52]	R. Kotaba et al., 'Algorithms for RIS-based Localisation and Sensing (Intermediary Specifications)", Deliverable D5.2 of the RISE-6G Project, June 2022
[RISED53]	B. Denis et al., 'Control for RIS-based localisation and sensing (Final Specifications)", Deliverable D5.3 of the RISE-6G Project, June 2023
[SDB23]	S. Sardellitti, P. Di Lorenzo, S. Barbarossa, "RIS-aided wireless fingerprinting localization based on multilayer graph representations," to be submitted on IEEE Communic. Letters, 2023.
[SFS+18]	Y. Sun, T. Fei, F. Schliep, and N. Pohl, "Gesture classification with handcrafted micro-Doppler features using a FMCW radar," in 2018 IEEE MTT-S International Conference on Microwaves for Intelligent Mobility (ICMIM), Munich, Germany, Apr. 2018
[SGD+17]	A. Shahmansoori, G. E. Garcia, G. Destino, G. Seco-Granados, H. Wymeersch, "Position and orientation estimation through millimeter-wave MIMO in 5G systems," *IEEE Transactions on Wireless Communications*, vol. 17, no. 3, pp. 1822-1835, 2017.
[SWS+19]	B. Sun, C. Wu, J. Shi, H. -L. Ruan and W. -Q. Ye, "Direction-of-Arrival Estimation Under Array Sensor Failures with ULA," in IEEE Access, vol. 8, pp. 26445-26456, 2020, doi: 10.1109/ACCESS.2019.2959274.
[SWC+22]	R. Sun, W. Wang, L. Chen, G. Wei and W. Zhang, "Diagnosis of Intelligent Reflecting Surface in Millimeter-Wave Communication Systems," in IEEE Transactions on Wireless Communications, vol. 21, no. 6, pp. 3921-3934, June 202.
[TCG+20]	H. Taghvaee, A. Cabellos-Aparicio, J. Georgiou and S. Abadal, "Error Analysis of Programmable Metasurfaces for Beam Steering," in IEEE Journal on Emerging and Selected Topics in Circuits and Systems, vol. 10, no. 1, pp. 62-74, March 2020.
[TLR04]	R. S. Thomä, M. Landmann, A. Richter, "RIMAX—A maximum likelihood framework for parameter estimation in multidimensional channel sounding," in *Proceedings of the International Symposium on Antennas and Propagation (ISAP'04)* pp. 53-56, 2004.
[WD20]	H. Wymeersch and B. Denis, "Beyond 5G wireless localization with reconfigurable intelligent surfaces," in ICC 2020 IEEE Inter. Conf. On Communic. (ICC), 2020, pp. 1–6.
[WHD+20]	H. Wymeersch, J. He, B. Denis, A. Clemente, and M. Juntti, "Radio localisation and mapping with reconfigurable intelligent surfaces: Challenges, opportunities, and research directions," IEEE Veh. Technol. Mag., vol. 15, no. 4, pp. 52–61, Dec. 2020.
[WLW+18]	Wen, F., Liu, P., Wei, H., Zhang, Y., & Qiu, R. C. (2018). Joint azimuth, elevation, and delay estimation for 3-D indoor localisation. *IEEE Transactions on Vehicular Technology, 67*(5), 4248-4261.
[WS20]	Wymeersch, Henk, and Gonzalo Seco-Granados. "Adaptive detection probability for mmWave 5G SLAM." 2020 2nd 6G Wireless Summit (6G SUMMIT). IEEE, 2020.
[WSD+21]	Wymeersch, H., Shrestha, D., De Lima, C. M., Yajnanarayana, V., Richerzhagen, B., Keskin, M. F., ... & Parkvall, S. (2021, September). Integration of communication and sensing in 6g: a joint industrial and academic perspective. In *2021 IEEE 32nd Annual International Symposium on Personal, Indoor and Mobile Radio Communications (PIMRC)* (pp. 1-7). IEEE.
[WSY20]	Wen, Fuxi, Hing Cheung So, and Henk Wymeersch. "Tensor decomposition-based beamspace esprit algorithm for multidimensional harmonic retrieval." In ICASSP 2020-2020 IEEE International Conference on Acoustics, Speech and Signal Processing (ICASSP), pp. 4572-4576. IEEE, 2020.
[XYS22]	L. Xie, X. Yu, and S.H. Song, "Intelligent reflecting surface-aided maneuvering target sensing: True velocity estimation", arXiv preprint https://arxiv.org/abs/2208.00198 (2022)

Document:	H2020-ICT-52/RISE-6G/D5.4		
Date:	29/09/2023	**Security:**	Public
Status:	Final	**Version:**	1.0

[ZCB+23]	Zheng, Pinjun, Hui Chen, Tarig Ballal, Mikko Valkama, Henk Wymeersch, and Tareq Y. Al-Naffouri. "JrCUP: Joint RIS Calibration and User Positioning for 6G Wireless Systems." arXiv preprint arXiv:2304.00631 (2023).
[ZHZ22]	J. Zhang, X. Hu and C. Zhong, "Phase Calibration for Intelligent Reflecting Surfaces Assisted Millimeter Wave Communications," in IEEE Transactions on Signal Processing, vol. 70, pp. 1026-1040, 2022.
[ZWD+22]	Z. Zhang, L. Wu, J. Dang, B. Zhu, and L. Wang, "Multiple RSS fingerprint based indoor localization in RIS-assisted 5G wireless communication system," The Inter. Archives of Photogr., Remote Sensing and Spatial Inform. Sciences, vol. 46, pp. 287–292, 2022.
[ZZD+21]	Zhang, Haobo, Hongliang Zhang, Boya Di, Kaigui Bian, Zhu Han, and Lingyang Song. "Metalo-calization: Reconfigurable intelligent surface aided multi-user wireless indoor localization." IEEE Transactions on Wireless Communications 20, no. 12 (2021): 7743-7757.